Published in final edited form as:

Nature. 2023 July ; 619(7970): 640–649. doi:10.1038/s41586-023-06219-w.

Structural insights into BCDX2 complex function in homologous recombination

Yashpal Rawal[1,7], **Lijia Jia**[1,7], **Aviv Meir**[2,7], **Shuo Zhou**[1], **Hardeep Kaur**[1], **Eliza A. Ruben**[1], **Youngho Kwon**[1], **Kara A. Bernstein**[3], **Maria Jasin**[4], **Alexander B. Taylor**[1], **Sandeep Burma**[1,5], **Robert Hromas**[6], **Alexander V. Mazin**[1], **Weixing Zhao**[1], **Daohong Zhou**[1], **Elizabeth V. Wasmuth**[1], **Eric C. Greene**[2,*], **Patrick Sung**[1,*], **Shaun K. Olsen**[1,*]

[1]Department of Biochemistry & Structural Biology, University of Texas Health Science Center at San Antonio, San Antonio, TX, 78229, USA

[2]Department of Biochemistry and Molecular Biophysics, Columbia University Irving Medical Center, New York, New York 10032, USA

[3]Department of Biochemistry & Biophysics, University of Pennsylvania School of Medicine, Philadelphia, Pennsylvania, 19104

[4]Developmental Biology Program, Memorial Sloan Kettering Cancer Center, New York, New York, 10065.

[5]Department of Neurosurgery, University of Texas Health Science Center at San Antonio, San Antonio, TX, 78229, USA

[6]Department of Medicine, University of Texas Health Science Center at San Antonio, San Antonio, TX, 78229, USA

Abstract

Homologous recombination (HR) fulfils a pivotal role in the repair of DNA double-strand breaks and collapsed DNA replication forks[1]. HR depends on several RAD51 paralogs, including the tetrameric complex of RAD51B, RAD51C, RAD51D, and XRCC2 (BCDX2)[2]. Despite its importance, the mechanism by which BCDX2 promotes RAD51 presynaptic filament assembly during HR remains unclear. Here, we report cryo-EM reconstructions of human BCDX2 in apo and ssDNA-bound states at 2.3 Å and 3.1 Å resolution, respectively. The structures reveal how the amino-terminal domains of RAD51B, RAD51C, and RAD51D participate in inter-subunit interactions that underpin complex formation and single-stranded DNA binding specificity. Importantly, single-molecule DNA curtain analysis yields insights into how BCDX2 enhances

[*]Correspondence and requests for materials should be addressed to E.C.G. (ecg2108@cumc.columbia.edu), P.S. (sungp@uthscsa.edu), or S.K.O. (olsens@uthscsa.edu).

[7]These authors contributed equally to this work

Author Contributions

Protein purification was conducted by Y.R and H.K. Structural experiments and analysis were conducted by L.J., E.V.W., and S.K.O. Y.R. conducted biochemical, mass photometry and negative stain EM assays. S.Z. conducted SPR assays. A.M. conducted single-molecule experiments. K.A.B., M.J., Y.K., R.H., A.B.T., S.B., A.V.M., W.Z, and D.Z. assisted with experimental design and data interpretation. The figures and manuscript were prepared by Y.R., L.J., A.M., Y.K., E.V.W., E.C.G., P.S., and S.K.O., with input from all authors.

Competing Interests

The authors declare no competing interests.

the assembly of the RAD51-ssDNA nucleoprotein filament crucial for HR execution. Moreover, our cryo-EM and functional analyses explain how RAD51C mutations found in cancer patients[3–6] inactivate DNA binding and the HR mediator activity of BCDX2. Altogether, our findings shed light on the role of BCDX2 in HR and provide the requisite foundation for understanding how pathogenic mutations in BCDX2 impact genome repair.

Keywords

DNA repair; cryo-electron microscopy; single-molecule analysis; homologous recombination; RAD51; BCDX2

Failure to remove DNA lesions induced by environmental and endogenous agents can cause cell death and potentially compromise genome integrity and lead to neoplastic transformation of cells[7]. DNA double-strand breaks (DSBs) are among the most deleterious of all such lesions, as a failure to eliminate them can lead to the types of gross chromosomal rearrangements found in cancer cells[8]. Homologous recombination (HR) is a major DSB repair pathway that is highly accurate as the process is directed by a homologous DNA template.

In HR, DSB ends are processed to generate a long 3’ overhanging ssDNA tail that serves as the platform for the assembly of the machinery that catalyzes repair[1]. Specifically, once formed, the ssDNA tail is rapidly coated by replication protein A (RPA), which prevents the formation of ssDNA secondary structures and spurious DNA degradation. RPA is subsequently replaced by the recombinase RAD51 to assemble a nucleoprotein filament, referred to as the presynaptic filament, capable of conducting DNA homology search and strand invasion upon location of homology[9]. RPA-RAD51 exchange on ssDNA is facilitated by HR mediator proteins[2,10].

Six RAD51 paralogs, namely, RAD51B, RAD51C, RAD51D, XRCC2, XRCC3, and SWSAP1, exist in humans, and they form distinct complexes that play a crucial role in HR by acting as mediators of RAD51 presynaptic filament assembly[2]. Based on amino acid sequence analysis and structure prediction, these paralogs harbor a conserved ATP binding domain, and with the exception of XRCC2 and SWSAP1, a globular N-terminal domain (NTD) of unknown function[2]. Three RAD51 paralog complexes have been described, specifically, the tetrameric BCDX2 (RAD51B, RAD51C, RAD51D, and XRCC2) complex, the dimeric CX3 (RAD51C and XRCC3) complex[11] and the dimeric SWSAP1-SWS1 complex[12]. In humans, BCDX2 is required for DSB repair in vivo, and elimination of any individual subunit renders cells hypersensitive to DNA damaging agents and reduces DNA damage-induced RAD51 foci formation[5,13]. Mutations in genes that encode RAD51B, RAD51C and RAD51D, are found in cancer patients[3–6] and mutations in RAD51C and XRCC2 are associated with the cancer prone syndrome Fanconi anemia[14] and accordingly, these genes are also known as FANCO[15,16] and FANCU[17], respectively.

There is currently no structural information on any of the three human RAD51 paralog complexes, and there are glaring knowledge gaps regarding the mechanisms by which these protein complexes promote RAD51 presynaptic filament assembly. Herein, we have

achieved cryo-EM reconstructions of the human BCDX2 complex in apo and ssDNA-bound states with nominal resolutions of 2.3 and 3.1 Å, respectively. The structures reveal the organization of the RAD51 paralogs and provides important insights into the nucleotide dependence and DNA substrate specificity profile of this complex. Notably, the RAD51B, RAD51C, and RAD51D amino-terminal domains (NTDs) participate in extensive inter-subunit interactions, including tripartite networks that underpin BCDX2 complex assembly and that the unique configuration of NTDs within the complex confers ssDNA specificity through steric occlusion. Our BCDX2 reconstruction provides the basis for understanding the structural relevance of cancer patient-derived mutations in BCDX2 subunits, which we highlight through analysis of RAD51C mutations found in ovarian, breast, and lung cancers. Mechanistic insights are provided by a combination of biochemical and biophysical methods, including single-molecule studies revealing how BCDX2 mediates RPA-RAD51 exchange on ssDNA. Collectively, our studies provide mechanistic insights into the HR mediator function of BCDX2, the molecular basis by which BCDX2 mutations lead to disease, and provide the foundation for targeting the BCDX2 complex for therapeutic intervention in cancer.

High-resolution cryo-EM structure of human BCDX2

We co-expressed full-length human RAD51B, RAD51C, RAD51D, and XRCC2 in insect cells using a single macrobaculovirus and purified the tetrameric BCDX2 complex in the presence of ATP/Mg^{2+}, needed to maintain stability of the tetrameric complex, to near homogeneity (Extended Data Fig. 1a). Analysis by mass photometry confirmed the monodispersity of BCDX2 as a ~150 kDa complex and, consistent with previous results[11], also revealed the dissociation of the complex upon omission of ATP/Mg^{2+} (Extended Data Fig. 1b). Unless otherwise noted, all biochemical and biophysical assays described in this manuscript were performed in the presence of ATP/Mg^{2+} whereas samples subjected to cryo-EM analysis were exchanged into buffer containing AMP-PNP/Mg^{2+} prior to grid preparation and data acquisition. We were able collect high quality cryo-EM data to generate a three-dimensional (3D) map of BCDX2 with a nominal resolution of 2.3 Å (masked) that provides detailed information regarding complex architecture and significant functional insights (Extended Data Fig. 1c and 2a–c; Extended Data Table 1). We hereafter refer to this structure as ‘apo BCDX2’ to distinguish it from the ssDNA-bound structure we report below. In the apo BCDX2 structure, RAD51D interacts on either side of its ATP binding domain with the ATP binding domains of RAD51C and XRCC2 (Fig. 1). The NTDs of RAD51B, RAD51C, and RAD51D decorate the periphery of the complex with each NTD being in close contact with both the ATPase domain and NTD of the neighboring subunit, while XRCC2, which lacks an NTD, associates with the ATP binding domain of RAD51D and the NTDs of RAD51C and RAD51D (Fig. 1). There was clear density for nucleotides within the ATP binding sites of RAD51C (ADP), RAD51D (AMP-PNP), and XRCC2 (AMP-PNP) (Fig. 1a; Extended Data Fig. 2d, e). The extensive network of interactions between RAD51C, RAD51D, and AMP-PNP at the RAD51C/RAD51D interface, which will be described in greater detail below, likely explains the observed dependence of BCDX2 complex stability on ATP/Mg^{2+} (Extended Data Fig. 1b)[6]. While the NTD and linker

region of RAD51B are well-ordered, its predicted ATP binding domain is not visible in our cryo-EM maps (Fig. 1), likely because it is highly dynamic.

Unique NTD configuration and interaction network in BCDX2

Despite sharing only 16–28% overall sequence identity [18], the structures of the ATP binding and N-terminal domains (NTDs) of BCDX2 subunits and RAD51 are highly similar. The ATPase domains of RAD51 and BCDX2 subunits superimpose with root mean square deviations (RMSDs) of between 1.5 to 3.1 Å (Extended Data Table 2) while the NTDs superimpose with RMSDs of between 1.7 to 2.1 Å (Extended Data Table 3). The major structural difference between the BDCX2 subunits and RAD51 is the orientation of the NTD relative to the ATPase domain (Fig. 2). While the NTD of RAD51 folds back towards its ATPase domain at an approximate 90° angle and participates in a small network of interactions with the ATPase domain, the NTDs of RAD51C and RAD51D project away from their ATPase domains at an approximate 45° angle which prevents intramolecular interactions (Fig. 2). As such, while the NTDs of RAD51 protomers within the presynaptic filament make few contacts with neighboring subunits (PDB 7EJC)[19], the NTDs of RAD51B, RAD51C, and RAD51D show extensive interactions with both the NTDs and ATPase domains of neighboring subunits within the BCDX2 complex.

Interestingly, even though the NTDs of RAD51B, RAD51C, and RAD51D all project away from their ATP binding domains (Fig. 2a, left), the NTDs themselves each adopt drastically different spatial orientations relative to their corresponding ATPase domains (Fig. 2a, right). As noted above, the NTDs of RAD51B, RAD51C, and RAD51D harbor a conserved structure comprised of four α-helices (H1-H4) and, surprisingly, structural comparison reveals rigid body rotations between 51° and 165° and translations of 3 to 8 Å relative to the ATPase domains (Fig. 2a, right). As such, entirely different NTD surfaces of the RAD51 paralogs are involved in the intermolecular interactions within the BCDX2 complex (Extended Data Fig. 3) revealing a prominent network of tripartite interactions involving Pro18 of the RAD51C NTD, Leu36, Met39, and Tyr46 of the RAD51B NTD and Phe176 and Leu226 from the ATPase domain of RAD51D (Fig. 2b).

RAD51 possesses a crucially important protein polymerization motif spanning residues Phe86 to Ala89 (referred to as the FXXA motif)[20,21]. Specifically, the side chains of Phe86 and Ala89 insert into hydrophobic pockets on the surface of adjacent subunits within the RAD51 filament (Fig. 2c–e). As such, the F86E and A89E RAD51 mutants fail to self-associate or form nuclear foci upon DNA damage occurence[20,22]. RAD51 paralogs lack the FXXA motif, particularly at the residue corresponding to Phe86 of RAD51, with Met64 in RAD51B, Lys84 in RAD51C, Pro65 in RAD51D, and His6 within the disordered N-terminal region of XRCC2, replacing Phe86 of RAD51 (Fig. 2c–e). Importantly, regions of BCDX2 subunits corresponding to the hydrophobic pocket that accommodates Phe86 within the RAD51 presynaptic filament are almost completely filled by bulkier hydrophobic and charged side chains (Fig. 2e, f). In RAD51B, for example, Tyr180, Arg191, and Glu198 replace Ala192, Leu203, and Met210 of RAD51, and AlphaFold modeling shows that this results in a much shallower and charged pocket that would severely clash with a phenylalanine (Fig. 2f). Taken together, our structural analysis reveals crucial differences

that underpin the oligomeric structure of the BCDX2 complex in relation to the RAD51 filament.

BCDX2 active sites and catalytic activity

Two Mg^{2+}-coordinated AMP-PNP molecules are observed, one at the interface between XRCC2 and RAD51D in the XRCC2 active site and the other at the interface between RAD51D and RAD51C in the RAD51D active site (Fig. 3a). The AMP-PNP molecules are nearly completely buried at these conserved interfaces, with ~83% of total accessible surface area being occluded from solvent. The adenine of AMP-PNP is sandwiched by Glu56 and Arg91 of XRCC2 and Pro302 in RAD51D (Fig. 3a, b). A similar arrangement is observed for the AMP-PNP bound to the RAD51D active site with Gln115 and Arg145 of RAD51D and Lys333 of RAD51C sandwiching the adenine (Fig. 3a, b). Overall, these AMP-PNP contacts closely resemble those observed for the ATPase site of RAD51[19,23,24]. Backbone amide groups of P-loop residues and Mg^{2+} interact with the β-phosphate of AMP-PNP bound to both the RAD51D and XRCC2 active sites. A conserved and mechanistically important network of contacts is observed between the γ-phosphate of AMP-PNP and lysine residues from the ATP binding site (Lys113 in RAD51D and Lys54 in XRCC2), lysine residues from adjoining subunits that contact ATP in *trans* (Lys328 in RAD51C and Lys297 of RAD51D), and Mg^{2+} (Fig. 3a, b). The two ordered Mg^{2+} ions are coordinated by conserved threonine residues within the Walker A motif (Thr114 in RAD51D and Thr52 in XRCC2) (Fig. 3a, b).

The constellation and identity of most of the amino acids within the active sites of XRCC2 and RAD51D are conserved within RAD51C, but a key difference is that there are no *trans* contacts to the nucleotide due to the disorder of RAD51B (Fig. 3a, b). While the ATPase domains of XRCC2, RAD51D, and RAD51C are all buttressed by contacts to both the ATPase domains and NTDs of neighboring subunits, RAD51B is at the ‘bottom’ of the complex and there is no NTD from a preceding subunit to stabilize its ATPase domain (Fig. 1). We surmise that the intrinsically more flexible nature of the RAD51B ATPase domain is due to lack of NTD stabilization. We speculate that the presence of ADP in the RAD51C ATP binding site is the result of hydrolysis that occurred during BCDX2 purification in the presence of ATP/Mg^{2+} and that ADP in the RAD51C active site was not displaced by AMP-PNP during sample preparation for cryo-EM due to flexibility of the RAD51B ATP binding domain, and thus, lack of *trans* contacts to the γ-phosphate.

We have previously reported that BCDX2 hydrolyzes ATP in a manner stimulated by DNA-binding[6]. To further investigate contributions of individual subunits of this complex in ATP hydrolysis, we purified RAD51B-RAD51C (BC) and RAD51D-XRCC2 (DX2) sub-complexes for testing. Consistent with structural analysis showing ADP densities at RAD51C walker A motif and AMP-PNP or ATP densities at RAD51D and XRCC2 Walker A motifs, BC but not DX2 displayed ATPase activity with a dependence on ssDNA. Together with the structural information, these results suggest that the ATP hydrolytic center of BCDX2 resides within RAD51B and/or RAD51C. Interestingly, DNA-stimulated ATP hydrolysis observed upon mixing BC and DX2 was consistently lower than BC alone, suggesting that DX2 downregulates ATP hydrolysis by BC (Fig. 3c). A conserved lysine

residue in the Walker A motif of ATPases including human RAD51 is critical for ATP binding as well as hydrolysis [25]. Moreover, patient derived mutations in and around the Walker A motif of RAD51C have been shown to reduce ATP hydrolysis by BCDX2[6]. Here we examined the effect of mutating the conserved lysine residue K131 located in the Walker A motif of RAD51C. Importantly, while the RAD51C^{K131A} mutation has no effect on BCDX2 complex stability, it greatly impairs its ATPase activity (Fig 3d).

Basis for BCDX2 DNA substrate binding and specificity

Previously, we demonstrated that BCDX2 binds ssDNA with high affinity[26]. Here, we have sought to gain insights into the location of the DNA substrate binding site of BCDX2 and the basis for ssDNA binding specificity. Two flexible loops, L1 and L2, within RAD51 provide the majority of contacts with ssDNA and dsDNA in pre- and post-synaptic complexes within the RAD51 presynaptic filament, respectively[19,24,27]. Analysis of surface electrostatics of our BCDX2 structure reveals a highly basic surface formed in large part by L1 and L2 of RAD51C and RAD51D, which resemble that of nucleofilaments of RAD51 (Fig. 4a)[19,24,28]. This basic surface is extended on one side of the core RAD51C/D module by XRCC2 L1 and L2, and docking of the RAD51B ATPase domain onto RAD51C shows that the basic surface extends along RAD51B on the other side of BCDX2 (Fig. 4a; Extended Data Fig. 3h).

We subsequently determined a cryo-EM structure of BCDX2 in complex with poly(C) ssDNA at a nominal resolution of 3.1 Å (masked) (Fig. 4b–e; Extended Data Fig. 4 and 5; Extended Data Table 1). In our structure, unambiguous density for the sugar-phosphate backbone and nitrogenous bases of six nucleotides was evident that spans a contiguous basic surface on the RAD51C, RAD51D, and XRCC2 subunits of BCDX2 (Fig. 4b). Consistent with this observation, we found that while BC and DX2 subcomplexes alone exhibit no appreciable DNA binding, mixing these entities leads to robust enhancement of DNA binding (Fig. 4f). Moreover, while BCD heterotrimer lacking XRCC2 displays modest DNA binding activity, the DNA binding activity of CDX2 heterotrimer lacking RAD51B is comparable to that of the complete BCDX2 complex (Fig. 4f). Our biochemical analysis thus provides support to the premise that RAD51C-RAD51D interactions underpin a ssDNA binding interface in BCDX2 that is bolstered by XRCC2. Our data show that optimal DNA binding activity requires both BC and DX2 (Fig. 4f, g), and the latter attenuates ssDNA-dependent ATP hydrolysis by BC (Fig. 3c). It is plausible that DX2, by attenuating ATP hydrolysis by BC, increases the resident time of the tetrameric BCDX2 ensemble on RPA-ssDNA to allow for RPA-RAD51 exchange on the ssDNA to facilitate the assembly of presynaptic filament. Like apo BCDX2, the putative ATPase domain of RAD51B is not visible in the BCDX2/ssDNA structure indicating that ssDNA binding alone fails to induce or stabilize contacts between the RAD51B and RAD51C ATPase domains. There was also clear density for AMP-PNP within the ATP binding sites of RAD51D and XRCC2 as in apo BCDX2 (Extended Data Fig. 5d). In contrast to apo BCDX2 in which the ATP binding site of RAD51C is bound to ADP as noted above (Extended Data Fig. 2d), density consistent with AMP-PNP is present in the ATP binding site of RAD51C ssDNA-bound BCDX2 (Extended Data Fig. 5d).

Residues from RAD51D and XRCC2 contact four and three nucleotides of the ssDNA, respectively. Nearly all residues contacting the sugar phosphate backbone of the ssDNA are located within L2s of RAD51C, RAD51D, and XRCC2 (Fig. 4b, c, e). Backbone amide nitrogen atoms of Arg253, Leu 264, Gly265, and Arg266 of RAD51D and Gln200 of XRCC2 and the side chains of Thr259 and Ser304 of RAD51C, Arg266 of RAD51D, and Arg224 of XRCC2 participate in hydrogen bonds to the phosphate backbone of ssDNA (Fig. 4b). Nearly all contacts to the cytosine bases of the ssDNA are mediated by the side chains of residues located in L1s of RAD51C, RAD51D, and XRCC2 (Fig. 4b, e). The side chains of Ser256 of RAD51C, Arg221 and Arg253 of RAD51D, and Arg159 of XRCC2 engage in hydrogen bond-mediated contacts to the cytosine bases of the ssDNA. Accordingly, BCDX2 complexes reconstituted by mixing purified WT BC with DX2 carrying either the R266A mutation in RAD51D or R159A mutation in XRCC2 strongly or moderately impairs DNA binding, respectively (Fig. 4g). Notably, comparable DNA binding activity was seen in BCDX2 purified as a tetramer or reconstituted by mixing WT BC with DX2 (Fig. 4g). Additional patchy density projects from the 3’ end of the ssDNA included in the final model towards Arg249 and Arg258 of RAD51C (Fig. 4b, c). This suggests weak interactions between RAD51C and one or two additional nucleotides at the 3’ end of the ssDNA continuing along the conserved basic surface of BCDX2.

Comparison of ssDNA-bound BCDX2 and RAD51 structures shows that although the basic patch comprising the DNA substrate binding site is well-conserved, there are several significant differences in how ssDNA is engaged (Fig. 4c, d, e). This includes significant diversity of L1 and L2 residues involved in contacts to ssDNA and differences in the ssDNA paths, particularly at the 5’ end (Fig. 4b, c, d, e). While RAD51 binds ssDNA in nucleotide triplets with L2 inserted into the space between triplet repeats [24], BCDX2 engages ssDNA in a less regular manner without such a role for L2s (Fig. 4b, e). Furthermore, residues involved in contacts to nucleotides in the RAD51/ssDNA structure are very poorly conserved in BCDX2 subunits (0–23% identity; 20–36% similarity) and there are more contacts to the nitrogenous bases in the BCDX2/ssDNA structure (Fig. 4b, e). Also notable is the lack of conservation of RAD51 Arg235 in BCDX2 subunits, which is involved in dsDNA engagement and DNA strand exchange by RAD51 (Fig. 4e) (PDB: 7EJE)[19]. Lastly, there is variability in the length of L1, with RAD51B and XRCC2 being two residues and one residue longer than the corresponding loop in RAD51 and RAD51C and RAD51D being three and two residues shorter, respectively (Fig. 4e).

We next sought to gain insights into the basis of BCDX2 specificity for ssDNA and for the altered path of ssDNA in the BCDX2 and RAD51 structures. To that end, we superimposed the RAD51C ATPase domain onto the RAD51 subunit contacting the 3’ end of ssDNA in the presynaptic RAD51-ssDNA complex (Extended Data Fig. 6a, b). While the ATPase domains of RAD51C and RAD51 superimpose well (RMSD= ~1.5 Å), analysis of the superposition reveals substantial differences in the positioning of subsequent subunits of BCDX2 and RAD51 complexes relative to each other (Extended Data Fig. 6a, b). While most ATPase domain/ATPase domain contacts and/or composite ATP interactions at the interface between RAD51C/D, RAD51D/XRCC2, and RAD51 subunits are conserved (Fig. 3a, b; Extended Data Fig. 7), the RAD51C linker and ATPase domain of RAD51D tilt as a rigid body by ~11° relative to the second RAD51 subunit in the superposition (RAD51.2;

Extended Data Fig. 6a). An even greater ~23° rigid body tilting of the RAD51D linker and XRCC2 ATPase domain relative to the third RAD51 subunit in the superposition is observed (RAD51.3; Extended Data Fig. 6b).

Superposition of the postsynaptic RAD51/dsDNA structure[19,24] onto our BCDX2/ssDNA structure reveals significant clashes that occur between the complementary DNA strand with L1 of XRCC2 (Extended Data Fig. 6c). These clashes stem from the tilting of BCDX2 subunits relative to RAD51 described above and from structural differences within and in proximity to L1 of XRCC2, including an extension and altered orientation of H12, which imparts rigidity to this region (Extended Data Fig. 6b, d). Though clashes occur with ssDNA and dsDNA in the model, the higher flexibility of ssDNA very likely allows it to sample different paths within the DNA binding groove of BCDX2 (Fig. 4c, d). This is particularly evident at the 5' end of the ssDNA in the BCDX2/ssDNA structure in which the backbone of the first three ordered nucleotides are flipped nearly 180 degrees relative to the RAD51/ssDNA structure, thereby circumventing the most severe steric clashes that would occur based on the RAD51 ssDNA path (Fig. 4c, d). In contrast, dsDNA is bulkier and less flexible and sampling of available paths would therefore be restricted by L1 of XRCC2 and by the congregation of NTDs in proximity to this loop (Extended Data Fig. 6c).

Single-molecule DNA curtain analysis of HR mediator activity of BCDX2

We employed single molecule DNA curtain analysis to define the role of BCDX2 as a HR mediator. For this, we constructed, expressed and purified GFP-tagged BCDX2 labeled on either the RAD51C or XRCC2 subunit. We could readily detect the association of BCDX2 with RPA-bound molecules of ssDNA in reactions containing ATP (Fig. 5a, b, c). In contrast, no BCDX2 binding activity was observed in reactions where ATP was omitted (Extended Data Fig. 8a). Surprisingly, the BCDX2 binding activity was transient (Fig. 5a, b), and reactions with GFP-tagged RAD51C (plus unlabeled RAD51B, RAD51D, XRCC2) and ssDNA bound by mCherry-RPA yielded a dissociation rate constant (k_{off}) of 0.471 min^{-1} with a 95% confidence interval (CI) of 0.433 to 0.510 (Fig. 5c). Similar results were obtained in reactions with either GFP-tagged XRCC2 or with unlabeled RPA (Fig. 5b, c). Strikingly, BCDX2 remained tightly bound to the RPA-ssDNA molecules when either of the non-hydrolysable ATP analogs ATPγS or AMP-PNP was included in the reaction, indicative of ATP hydrolysis playing a regulatory role in the turnover dynamics of BCDX2 (Extended Data Fig. 8a). Note, these assays can only be performed with RPA-ssDNA and not naked ssDNA, because RPA is essential for minimizing ssDNA secondary structure thus allowing the ssDNA molecules to be extended parallel to the sample chamber surface for visualization by TIRFM, as previously described [29]. RPA binds tightly to ssDNA with a picomolar binding affinity, yet it is still capable of undergoing rapid exchange when free RPA is present in solution [30]. Interestingly, although BCDX2 bound tightly to the RPA-ssDNA molecules, we found no evidence that it enhanced either the dissociation or exchange of RPA from the ssDNA (Fig. 5d, e, f).

We next assessed BCDX2 interactions with RAD51 filaments. We could find no evidence for BCDX2 interactions with pre-assembled RAD51 filaments, nor could we detect BCDX2 interactions with RAD51 filaments when BCDX2 and RAD51 were simultaneously co-

injected into reactions containing RPA-ssDNA (Extended Data Fig. 8b). However, when RAD51 was injected into reactions containing BCDX2 pre-bound to RPA-ssDNA we observed a 42% to 49% increase in the rate of mCherry-RPA dissociation (Fig. 5g, h, i), which serves as a reliable proxy for the rate of RAD51 filament assembly[31,32]. ATPgS and AMP-PNP appear to trap BCDX2 on RPA-ssDNA (Extended Data Fig. 8a), but the addition of RAD51 to these trapped complexes causes BCDX2 to dissociate allowing for concomitant RAD51 filament assembly (Extended Data Fig. 8c, d). However, the rate for RAD51 filament assembly only increased by 24% or 20% with ATPγS or AMP-PNP, respectively, highlighting the need for ATP hydrolysis to achieve full stimulation of RAD51 filament assembly (Extended Data Fig. 8d). Taken together, these results show that ATP binding is necessary for BCDX2 association with RPA-ssDNA, ATP hydrolysis contributes to the release of BCDX2 from RPA-ssDNA, and BCDX2 bound to RPA-ssDNA accelerates the rate of RAD51 filament formation, but BDCX2 does not remain bound to already assembled RAD51 filaments. While these data show clear evidence of BCDX2 binding interactions with the RPA-ssDNA molecules, they cannot distinguish between BCDX2 binding to ssDNA, RPA or both. However, our bulk biochemical and cryo-EM data both show that BCDX2 binds to naked ssDNA, so interpreted within this context, it is likely that the binding interactions observed in the DNA curtain assays reflect BCDX2 binding to the ssDNA itself.

Lastly, as a means to assess the relevance of the ssDNA binding pocket observed in our cryo-EM structure, we tested two mutations, RAD51D-R266A and XRCC2-R159A, both of which are predicted to disrupt interactions with ssDNA. Consistent with this prediction, we find that the BCDX2 complexes harboring either RAD51D-R266A or XRCC2-R159A show no appreciable binding to the RPA-ssDNA molecules in the DNA curtain assays (Fig. 5j, k).

EM analysis of the HR mediator attribute of BCDX2

Next, we analyzed RAD51 filaments formed with a 150-mer oligonucleotide in the presence or absence of BCDX2 complex by negative stain electron microscopy (Fig. 5j–l; Extended Data Fig 9a). Interestingly, the number of RAD51 nucleoprotein filaments per micrograph were significantly higher in the presence of BCDX2 vs RAD51 alone (Fig 5j). However, we did not observe any substantial increase in RAD51 filament length in the presence of BCDX2 (Fig. 5l). We also observed a significant increase in the number of interconnected RAD51 filaments in the presence of BCDX2 (Fig. 5k). These findings suggest that BCDX2 promotes RAD51 filament formation by increasing the local concentration of RAD51 and DNA, which is also supported by a previous study showing RAD51 filaments forming in proximity of BCDX2 bound DNA[11]. To further understand role of BCDX2 in RAD51 filament formation, we also tested the trimeric CDX2 subcomplex which can bind ssDNA almost as efficiently as BCDX2 (Fig 4f) but lacks RAD51B. Notably, CDX2 was unable to promote RAD51 filament formation (Fig 5j, k, l). The results thus reveal a key role of RAD51B in the promotion of RAD51 filament formation by BCDX2.

SPR analysis and AlphaFold modeling of BCDX2/RAD51 interactions

We surmised that the HR mediator activity of BCDX2 may entail its interaction with RAD51. To test this hypothesis, we conducted surface plasmon resonance (SPR) experiments with BCDX2 or its sub-complexes BC or DX2 immobilized on dextran SPR chips as an affinity matrix to test for possible RAD51 interaction (Fig. 6a–c). Interestingly, we observed RAD51 interaction with BCDX2 (Fig. 6a) and the BC sub-complex (Fig. 6b) with comparable affinities, whereas no interaction with the DX2 sub-complex (Fig 6c). RAD51 interactions with BCDX2 and its BC sub-complex were also validated by mass photometry analysis showing cumulative increase in molecular mass upon mixing RAD51 with BCDX2 or BC (Extended Data Fig. 9b, c). These results strongly suggest that the RAD51 interaction interface resides within the BC module of BCDX2. Moreover, we did not observe BCDX2 interaction with RPA (Fig 6d), suggesting that BCDX2 association with RPA coated DNA (Fig. 5a) is primarily through DNA binding by BCDX2.

We further investigated the basis for the BCDX2/RAD51 interaction based on our structural data and modelling. Our analysis revealed that it is unlikely that RAD51 interacts with BCDX on the XRCC2 side, as the structural elements of XRCC2 predicted to interact with ATP bound to a subsequent subunit are drastically different compared to RAD51 and other BCDX2 subunits. Salient changes include a substantial lengthening of a β-strand (β8) and altered conformation of a loop in this region of the structure (β7-β8 loop) that would lead to clashes with ATP (Extended Data Fig. 9d). In contrast, there is no structural impediment to interaction of RAD51 with BCDX2 on the RAD51B side. AlphaFold[33] modeling of RAD51B-RAD51C interaction (in the context of the BCDX2 structure) provided a high confidence model in which the ATPase domains are packed against each other similar to other subunits in the BCDX2 and RAD51 complexes (Fig. 6e). Importantly, modeling of RAD51-RAD51B interaction within the context of BCDX2 (Fig. 6e) also led to a high confidence model in which key structural elements of RAD51 pack against the ATP binding site of RAD51B, such that conserved *trans* interactions with ATP could occur. We note, however, that the buried surface area at the interface between the RAD51 and RAD51B ATPase domains is about a third of that observed for other neighboring subunits in the BCDX2 complex. We refer to this manner of RAD51/RAD51B interaction as ‘Mode 1’ and the resulting RAD51/BCDX2 model as ‘Model 1’ (Fig. 6e, f). Herein, XRCC2 is situated at the end of the ssDNA binding site, with a RAD51 nucleoprotein filament emanating from the bottom of the BCDX2 complex due to interactions between RAD51 and RAD51B (Fig. 6f).

We also considered mechanistic implications of the highly dynamic nature of the RAD51B ATPase domain. Accordingly, we modeled the standalone RAD51/RAD51B interaction (*e.g.*, not in the context of BCDX2 complex) which yielded a high confidence model in which key structural elements of RAD51B are positioned in proximity to the ATP binding site of RAD51 similar to RAD51B/RAD51C interaction (Fig. 6e). This “Mode 2” RAD51/RAD51B interaction model has ~1250 $Å^2$ of surface area buried at the interface between the ATPase domains of the constituents (Fig. 6e). This compares favorably to RAD51B/RAD51C (~1500 $Å^2$ buried surface area) and RAD51 filaments (~1000 $Å^2$ buried surface area) and is significantly greater than the ~560 $Å^2$ buried at the RAD51/RAD51B Mode

1 interface. Given the high flexibility of the RAD51B ATP binding domain, it is formally possible that this RAD51B domain endows BCDX2 with the ability to interact with RAD51 presynaptic filaments via Mode 1 and/or Mode 2. We refer to this RAD51/BCDX2 model as 'Model 2', which could impart structural plasticity to promote assembly of a nascent RAD51 filament on ssDNA, could be relevant at locations involving junctions between ssDNA and dsDNA during HR, and/or could facilitate recruitment of additional HR factors (Fig. 6g).

Effect of RAD51C cancer mutations on DNA binding

Previously, we demonstrated that patient-derived mutations in and around the Walker A ATP binding motif of RAD51C impair DNA binding and ATP hydrolysis by BCDX2 biochemically, and they also affect cellular viability and engender hypersensitivity to DNA damaging agents and defective HR[6] (Fig. 7a). As our cryo-EM analysis has provided evidence for RAD51C and RAD51D interactions being critical for BCDX2 complex formation and DNA binding, here, we focused on studying patient mutations in non-catalytic amino acid residues of RAD51C that cause strong defects in RAD51C and RAD51D interactions and HR in cell-based assays[6].

RAD51C-R258H is the only reported mutation for FA complementation group O[16], and RAD51C-R312W germline mutation leads to predisposition to breast and ovarian cancer[3,6,34]. Both mutations cause severe defects in HR in cell-based assays and in RAD51C-RAD51D interactions[6]. We found that these pathogenic mutations strongly impair DNA binding (Fig. 7b) and DNA-stimulated ATP hydrolysis (Fig. 7d; Extended Data Fig. 10) by the mutant BCDX2 complexes. In this regard, it is notable that RAD51C-R258 is equivalent to RAD51-R241[6], a key residue involved in DNA binding[24]. Both mutations abolish the ability of BCDX2 to interact with RPA-ssDNA molecules in the DNA curtain assays (Fig. 7c) and like WT BCDX2, mutant BCDX2 complexes do not interact with preassembled RAD51 filaments (Extended Data Fig. 8b). Importantly, both BCDX2 mutant complexes are devoid of the ability to promote RAD51-ssDNA nucleoprotein filament assembly (Fig. 7e, f, g; Extended Data Fig. 9a). We note that Arg258 and Arg312 of RAD51C are located proximal to cryo-EM density extending from the 3'-most modelled nucleotide in our BCDX2/ssDNA structure (Fig. 4b, c). Altogether, the data presented here suggest that pathogenicity of the RAD51C-R258H and RAD51C-R312W mutations likely stems from impairment of DNA binding through disruption of interactions with DNA nucleotides extending 3' along RAD51C within the conserved basic surface of BCDX2.

Altogether our work reveals the overall architecture and organization of the BCDX2 complex and important insights into the nucleotide dependence and DNA substrate specificity profile of this complex. Our results also provide insights into how DNA and ATP binding/hydrolysis relate to the dynamics of complex assembly and disassembly which in turn regulate BCDX2 function. Our single-molecule analysis indicates that BCDX2 binds to RPA-ssDNA in an ATP-dependent manner and that hydrolysis of ATP mediates BCDX2 dissociation. Accordingly, substitution of ATP with a non-hydrolyzable ATP analog leads to stable association of BCDX2 with the RPA-ssDNA complex. We have also shown that BCDX2 association with RPA-ssDNA significantly increases the rate of RAD51-

ssDNA nucleoprotein filament assembly. Overall, our results suggest that BCDX2 functions similarly to the *Saccharomyces cerevisiae* RAD51 paralog complex Rad55-Rad57 and the *C. elegans* paralog complex RFS-1/RIP-1 by stimulating Rad51-ssDNA nucleoprotein filament without any stable association with mature RAD51 filaments[35–37]. The key mechanistic difference distinguishing BCDX2 from Rad55-Rad57 and RFS-1/RIP-1 is that the latter two complexes do not stably interact with RPA-ssDNA, but instead co-bind to RPA-ssDNA with Rad51 to promote filament assembly and then quickly dissociate from the resulting Rad51-ssDNA complexes[35,36]. In contrast, we now show that human BCDX2 binds to RPA-ssDNA before the arrival of RAD51 to then stimulate RAD51 filament assembly, thus revealing a new mode of RAD51 paralog mechanism of action. While our SPR, mass photometry, and modeling analyses indicate that BCDX2 physically interacts with RAD51, the structural basis for this interaction and its functional impact on the HR mediator activity of BCDX2 remain to be determined. Also unknown is the role of the RAD51B ATPase domain in regulating the function of the BCDX2 complex. In sum, our work provides a significant step forward in our understanding of BCDX2 structure and function and lays the groundwork for answering remaining questions regarding how it and other RAD51 paralog complexes act as mediators of RAD51 presynaptic filament assembly during HR.

Methods

Protein expression and purification

BCDX2 purification was carried as previously described [6]. Briefly BCDX2 (RAD51B-His and XRCC2-Flag) was expressed in Hi5 insect cells using baculoviruses and all the purification steps were carried out at 0–4°C. Cell pellet was resuspended in T buffer (25 mM Tris-HCl, pH 7.5, 10% glycerol, 0.5 mM EDTA, 1mM DTT, 0.05% IGEPAL CA-630 (Sigma), 1 mM PMSF and protease inhibitors) containing 300 mM KCl (T300), 5 mM ATP, and 2 mM $MgCl_2$, lysed by sonication, clarified lysates was incubated with Ni-NTA resin and BCDX2 protein was eluted with T buffer containing 100 mM KCl (T100) with 200 mM Imidazole. For further purification protein was fractionated on HiTrap Q HP column with 150–600 mM KCl gradient and concentrated pooled fractions were subject to size exclusion chromatography in a Superdex200 Increase 10/300 GL column in T300 buffer with 2 mM each of ATP and $MgCl_2$. BCDX2 sample preparation for Cryo EM were otherwise carried out similarly except that size exclusion chromatography was performed in HEPES buffer without glycerol and IGEPAL CA-630 and with 50 mM KCl and 0.2 mM ATP and 1 mM $MgCl_2$. Peak fractions were concentrated and incubated with otherwise similar HEPES buffer but ATP replaced with 1 mM AMP-PNP for 3 hours and AMP-PNP was further enriched by buffer exchange during concentration.

For BC (RAD51B-His and RAD51C/GFP-RAD51C), BCD (RAD51B-His, RAD51C and RAD51D), DX2 (RAD51D and XRCC2-Flag/GFP-XRCC2-Flag) CDX2 (RAD51C, RAD51D and XRCC2-Flag) purification, crude cell lysates were prepared from 6–8 g cell pellet (from 800 ml insect cell culture) by sonication in 50 ml T300 with 5 mM ATP, and 2 mM $MgCl_2$, followed by centrifugation at 100,000 Xg for 60 min. For BC and BCD purification clarified lysate was incubated with 2.5 ml Ni-NTA resin (Qiagen, 1018142) for 1 hour, followed by sequential washes of the resin with 25 ml T300 buffer, 500 ml T buffer

with 1000 mM KCl (T1000) and 25 ml T100 buffer and with all the buffer also containing 20 mM imidazole, 2 mM each of ATP and $MgCl_2$. The BC and BCD complexes were eluted from the affinity matrix with 10 ml T100 buffer containing 200 mM imidazole and 2 mM each of ATP and $MgCl_2$. For DX2 and CDX2 purification clarified lysates were incubated with 1 ml anti-FLAG M2 resin (Sigma, A2220) for 2 hours, followed by sequential washes of the resin with 100 ml T300 buffer and 50 ml T100 buffer and with all the buffer also containing 2 mM each of ATP and $MgCl_2$. The DX2 and CDX2 complexes were eluted from the affinity matrix with 10 ml T100 buffer containing 200 ng/μl FLAG peptide (Sigma, F3290) and 2 mM each of ATP and $MgCl_2$. Further purification of each sub-complex was performed by ion exchange in a 1 ml HiTrap Q HP column fractionated with a 45 ml 150–600 mM KCl gradient in T buffer containing 2 mM each of ATP and $MgCl_2$. Peak fractions were pooled and concentrated to 0.4 ml in a Amicon 30 concentrator and then subject to size exclusion chromatography in a Superdex200 Increase 10/300 GL column in T300 buffer with 2 mM each of ATP and $MgCl_2$.

ULP1–6XHis, 6XHis-SUMO-RAD51 and untagged RPA complex were all overexpressed in E. coli BL21 (DE3) Rosetta2 by induction with 0.5 mM IPTG at $O.D._{600}$ 0.5–0.6 for overnight at 16°C. The crude cell lysates for ULP1–6XHis and 6XHis-SUMO-RAD51 were prepared from 20–25 g cell pellet (from 12 liter culture) by sonication in 100 ml T buffer containing 500 mM KCl (T500), followed by centrifugation at 100,000 Xg for 60 min. Each of clarified lysate was incubated with 5 ml Ni-NTA resin (Qiagen, 1018142) for 1 hour, followed by sequential washes of the resin with 25 ml T500 buffer, 250 ml T1000 buffer and 25 ml T100 buffer and with all the buffer also containing 20 mM imidazole. The ULP1–6XHis was eluted from the affinity matrix with 10 ml T100 buffer containing 200 mM imidazole, dialyzed overnight and concentrated. 6XHis-SUMO-RAD51 bound Ni-NTA resin was resuspended in 5 ml T100 buffer and 6XHis-SUMO tag was cleaved by incubating overnight with ULP1 on rotary shaker. RAD51 protein was eluted by collecting flowthrough and sequentially washing Ni-NTA resin in T100 buffer. Further purification RAD51 protein was fractionated with a 45 ml 150–450 mM KCl gradient in T buffer first by ion exchange in a 1 ml HiTrap Q HP column followed by 1 ml HiTrap heparin column with a 45 ml 150–450 mM KCl gradient in T buffer and peak fractions were concentrated and saved.

The crude cell lysates for RPA purification was prepared from 30–35 g cell pellet (from 12 liter culture) by sonication in 150 ml T100 buffer, Clarified lysates was fractionated through 25 ml Affi Gel Blue column with Sodium thiocyanate gradient (500–2000 mM, 5 CV) in T100 buffer, peak fractions were further fractionated through 10 ml MacroHAP hydroxyapatite column with phosphate gradient (10–180 mM, 6 CV) in T100 buffer, followed by fractionation with a 45 ml 150–450 mM KCl gradient in T buffer by ion exchange in a 1 ml HiTrap Q HP column and 1 ml HiTrap heparin column respectively and peak fractions were concentrated and saved.

All protein samples were snap frozen in liquid nitrogen and stored −80° C.

Cryo-EM sample preparation and data acquisition

Freshly eluted apo BCDX2 complex from a gel-filtration column (Superdex200 Increase 10/300 GL) was buffer exchanged to replace ATP with AMP-PNP and concentrated to ~6 μM. The sample was immediately applied onto cryo-EM Au grids (UltrAuFoil 1.2/1.3 300 mesh, Electron Microscopy Sciences) that had been glow discharged at 20 mA for 30 s in a Quorum EMS glow discharge machine. For the BCDX2/ssDNA complex, ~6 μM apo BCDX2 was mixed with a 10-fold molar excess of an 30-mer poly deoxycytidine oligonucleotide (5'-CCCCCCCCCCCCCCCCCCCCCCCCCCCCCC) in presence of 2 mM AMP-PNP. The mixture was incubated for 5 minutes at room temperature and then applied onto cryo-EM Au grids as for apo BCDX2. Grids were vitrified using a Vitrobot Mark IV (Thermo Fisher Scientific). Specifically, 3 ul of BCDX2 specimen was pipetted onto the grid maintained at 4°C and 100% humidity in the Vitrobot chamber. Grids were subsequently blotted for 3 s, with a blotting force of −10 and plunged into the liquid ethane. Grids were transferred into liquid nitrogen and stored at cryogenic temperatures before clipping, screening, and data collection.

Data collection was performed at 200 kV on a Glacios cryo-TEM microscope equipped with a Falcon IV camera and Selectris energy filter (slit width: 10 eV) at UT Health San Antonio Cryo-EM center. Imaging was acquired using Thermo Fisher Scientific's EPU software with an AFIS model. For apo BCDX2, a total of 1,741 image frames with EER file format were recorded with an exposure time of 7 s, a total dose of 51 $e^{-}/Å^2$ with a 5.65 e^{-}/pix/s dose rate; for the BCDX2/ssDNA complex, a total of 2,163 image frames with EER file format were recorded with an exposure time 8.99 s, a total dose of 52 $e^{-}/Å^2$ with a 4.47 e^{-}/pix/s dose rate. A total of 6,000 micrographs for BCDX2 and 7,000 micrographs for BCDX2/ssDNA were collected with a pixel size of 0.87 Å, a nominal magnification 130,000x, and a defocus range from −0.8 to −2.0 μm.

Cryo-EM data processing for apo and ssDNA-bound BCDX2

Post data collection, images were gain corrected, dose weighted, patch motion corrected using Cryosparc v3.3.1 [38]. The exact defocus value and CTF (Contrast Transfer Function) of each micrograph was estimated using Cryosparc's patch CTF estimation. For apo BCDX2 data processing, micrograph curation with a CTF resolution cutoff value of 5 Å resolution was applied to the data, and 5,600 micrographs were kept for particle picking. The blob picker function in Cryosparc was used for picking and yielded around 8,000,000 particles of 100 Å diameter. The particles were subsequently extracted at a 256 pix box size without downsampling. After three rounds of light 2D classification to filter noise and dissociated particles, 7,219,082 particles entered the next stages of 3D initial model reconstruction and 3D classification. Six *ab initio* models were generated in Cryosparc and were further used as initial references for heterogeneous refinement. For each cycle of heterogeneous refinement, the particles from the best class were kept for the next round of heterogeneous refinement. In total, 4 rounds of heterogeneous refinement were performed in Cryosparc, with the best class from the final heterogeneous refinement containing 1,192,629 particles. This class was refined to 3.0 Å with homogeneous refinement. A final step of stringent heterogeneous refinement was further applied using the 3.0 Å map as an initial model, which segregated

one class with improved resolution of 2.3 Å (based on FSC-0.143 criterion) using masked homogenous refinement. The final map, using a negative B-factor of −150 estimated in Cryosparc, was used for model building.

The BCDX2/ssDNA data processing workflow was similar, with micrograph curation of a CTF cutoff value of 5 Å resolution applied, around 4,000 micrographs were kept for particle picking. A set of around 4,000,000 particles with 256 pix box size were fed into 2D classification and 3,406,052 particles selected. These were used for 3D initial model generation with 6 classes and used four rounds of 3D heterogeneous refinement processing with 6 initial models as references. The final 3D heterogeneous refinement step retained 480,986 particles. This was followed by a further heterogeneous refinement with only 3 classes with one final class of 165,968 particles applied for homogeneous refinement, yielding a resolution of 3.12 Å. This was further refined using non-uniform refinement yielding a final resolution is 3.11 Å.

Model building and refinement

Models of RAD51B, RAD51C, RAD51D, and XRCC2, were first predicted using Alphafold2 [33]. After deleting the low confidence and disordered regions of each model, RAD51B, RAD51C, RAD51D, and XRCC2 were rigid-body docked into the cryo-EM map using UCSF ChimeraX [39]. All of the predicted models were fit with high confidence except the RAD51B ATP binding domain, which showed no density in our map. Fitting correlation values were 0.59 for RAD51C, 0.62 for Rad51D, and 0.65 for XRCC2. Further building and structural refinements were performed using COOT [40] and further refinements of stereochemistry and secondary structure were performed in PHENIX using phenix.real_space_refine [41]. For BCDX2/ssDNA model building, the model from the apo BCDX2 complex was directly fit into the cryo-EM map in ChimeraX, with a fitting correlation of 0.41. COOT was used for manually building the ssDNA molecule and PHENIX real space refinement used to refine the full BCDX2/ssDNA model. Both apo BCDX2 and BCDX2/ssDNA structural models were validated using wwPDB (https://validate-rcsb-2.wwpdb.org/). Figures for the cryo-EM map and models were prepared with ChimeraX [39] and PyMOL [42].

DNA binding and ATPase assays

For DNA binding, 1 nM of 5’ ^{32}P-labeled 80-nt ssDNA[43] was incubated with the indicated concentration of purified BCDX2 complex in 10 μl reaction buffer (50 mM Tris-HCl, pH 7.5, 155 mM KCl, 1 mM DTT, 1 mM ATP, 1 mM $MgCl_2$ and 100 ng/μl BSA) for 10 min at 37°C. Nucleoprotein complexes were resolved on 5% polyacrylamide gels in Tris-borate buffer (45 mM each). Gels were dried and subjected to phosphorimaging analysis with Amersham Typhoon phosphorimager (Cytiva) and the ImageQuant software (Cytiva).

BCDX2 complexes or its sub-complexes (1 μM) were incubated in the absence or presence of ssDNA (20 μM nucleotides, phiX174 virion) in 10 μl of reaction buffer (20 mM HEPES, pH 7.5, 1 mM DTT, 1 mM $MgCl_2$ and 30 mM KCl) containing 0.05 mM ATP with 0.25 μCi [γ–^{32}P] ATP at 37°C. Aliquots of 2 μl were withdrawn at the indicated times and

mixed with 2 μl of 0.5 M EDTA to stop the reaction. The level of ATP hydrolysis was determined by layer chromatography on PEI cellulose F sheets (Millipore, 105579) in 0.375 M potassium phosphate (pH 3.5), followed by phosphorimaging analysis.

Negative staining and electron microscopy

For presynaptic filament assembly, RAD51 (2μM) was incubated with 150-nt oligonucleotide (6μM nucleotides) with or without 25 nM BCDX2 variants in reaction buffer (25mM HEPES pH 7.5, 25mM KCl, 1 mM $MgCl_2$, and 2 mM ATP) at 37°C for 15 min. A droplet of 20 μl of a reaction mixture was loaded onto a glow-discharged carbon-coated 300 mesh copper grid (EMS CF300 cu) for 1min. After blotting with filter paper, the grid was immersed in a 20 μl droplet of the staining solution (2% uranyl acetate). The stain was removed from the grid by blotting with filter paper and the grid was washed with twice with water for 1min. Following excess stain removal, grids were dried in air for about 3 min. Negatively stained samples of hRAD51 presynaptic filaments were examined by transmission electron microscopy (TEM). Images were processed in Fiji ImageJ image analysis package and filaments were quantified using ImageJ plugin Ridge detection.

Mass photometry

Mass Photometry analysis was performed using a Refeyn TwoMP instrument (Oxford, UK). Contrast-to-mass calibration was achieved by standard curve covering mass range from 66 up to 480 KDa. The experiments were performed on sample carrier slides partitioned by six well silicone cassettes. BCDX2 purified in absence or in presence of 2 mM ATP and $MgCl_2$ each were diluted in 1X PBS buffer (137 mM NaCl, 2.7 mM KCl, 8 mM Na_2HPO_4, and 2 mM KH_2PO_4) to final concentration of 10 nM. For analyzing RAD51 interactions with BCDX2 or BC complexes, proteins were mixed in presence of 2 mM ATP and $MgCl_2$ each were diluted in 1X PBS buffer to final concentration of 5 nM each. Using AcquireMP software, blank acquisition field was first adjusted in native settings and then single particles were detected in a movie recorded for one minute at a 100 frames per second rate in ratiometric acquisition settings. All mass photometry data was analyzed with DiscoverMP software to produce mass values for each detected particle and plotted as normalized counts.

Surface Plasmon Resonance

Surface plasmon resonance experiments were performed using a Biacore T100 (with T200 sensitivity enhanced) equipped with a CM5 sensor chip. The ligand BCDX2 (148 kDa, >90% pure based on SDS–PAGE) was scouted for optimal pH and then immobilized using amine-coupling chemistry. The surfaces of flow cells were activated for 7 min with a 1:1 mixture of 0.1 M NHS (N-hydroxysuccinimide) and 0.4 M EDC (3-(N,N-dimethylamino) propyl-N-ethylcarbodiimide) at a flow rate of 5 μl/min. The ligand (BCDX2) at a concentration of 50 μg/ml in 10 mM sodium acetate, pH 5.0, was immobilized at a density of around 200 RU and one flow cell was left blank to serve as a reference surface. All surfaces were blocked with a 7 min injection of 1 M ethanolamine, pH 8.0. To collect kinetic binding data, the analyte RAD51 in 10 mM HEPES, pH 7.4, 150 mM NaCl, 1 mM ATP, 1 mM DTT, 1mM MgCl2, 0.05% Surfactant P20, pH 7.4, was injected over all flow cells

at various concentrations as shown in Figure 6a and b at a flow rate of 30 μl/min and at a temperature of 25°C. The complex was allowed to associate and dissociate for 60 and 600 s, respectively. Duplicate injections (in increasing concentration order) of each sample and a buffer blank were flowed over the two surfaces. Data were collected at a rate of 10 Hz. The data were fit to a heterogeneous ligand interaction model using the global data analysis option available within Biacore T200 evaluation software (Version 3.2.1).

Single molecule DNA curtain assays

All single molecule measurements were carried out at 37°C. Experiments were conducted with a custom–built prism–based total internal reflection fluorescence (TIRF) microscope (Nikon) equipped with 488nm laser (Coherent Sapphire, 200 mW) and a 561nm laser (Coherent Sapphire, 200 mW) [44]. Flow cells were assembled and ssDNA curtains were prepared as previously described [45,46]. ssDNA was generated using a 5' biotinylated primer annealed to M13 circular ssDNA as a template, by rolling circle replication with phi29 DNA polymerase [32]. The flow cell was attached to the microfluidic system and passivated with streptavidin containing lipid bilayer as described [31,44]. ssDNA was injected into the flow cell, attached to the lipid bilayer through biotin–streptavidin linkage, aligned at the barriers by application of a constant buffer flow, and secondary structures were disrupted by flushing 500 μL of 7 M urea in BSA buffer (40 mM Tris-Cl [pH 8.0], 2 mM $MgCl_2$, 1 mM DTT, and 0.3 mg/mL BSA) at a flow rate of 0.8 mL/min. Free ssDNA ends were anchored to the exposed pedestals through non-specific adsorption, as described [44].

BCDX2 binding to RPA filaments

Experiments were begun by flushing the ssDNA curtains with BSA buffer (40 mM Tris-Cl [pH 8.0], 2 mM $MgCl_2$, 1 mM DTT, and 0.3 mg/mL BSA) supplemented with 100 pM mCherry–RPA for 10 min at a flow rate of 0.8 mL/min. Then 10 nM BCDX2 (either GFP-BC plus DX2 or BC plus DX2-GFP, as indicated) was injected into the flow cells through 150 μL injection loop in HR buffer (30 mM Tris-Ac [pH 7.5], 100 mM KCl, 1 mM $MgCl_2$, 5 mM $CaCl_2$, 2.5 mM ATP (or 2.5 mM ATPγS, as indicated), 1 mM DTT, 0.2 mg/mL BSA at a flow rate of 0.15 mL/min. Data were collected continuously throughout the entire process at a rate of 1 frame per 10 seconds.

RAD51 filament assembly in the presence of BCDX2

RAD51 filament assembly was initiated by first binding BCDX2 to preassembled mCherry-RPA bound ssDNA curtains, as described above, followed by immediate injection of 500 nM RAD51 in HR buffer (30 mM Tris-Ac [pH 7.5], 100 mM KCl, 1 mM $MgCl_2$, 5 mM $CaCl_2$, 2.5 mM ATP (or 2.5 mM ATPγS or AMP-PNP, as indicated), 1 mM DTT, 0.2 mg/mL BSA at a flow rate of 0.15 mL/min. Data were collected continuously throughout the entire process at a rate of 1 frame per 3 seconds. Co-injection measurements were carried under the same conditions where 10nM BCDX2 was premixed with the 500nM RAD51 before injection into the flow-cell.

RPA exchange in the presence of BCDX2

Experiments were begun by connecting the flow-cells with two syringes, separated by a valve, containing either 100 pM mCherry-RPA or 100 pM unlabeled RPA in BSA buffer (40 mM Tris-Cl [pH 8.0], 2 mM $MgCl_2$, 1 mM DTT, and 0.3mg/mL BSA) supplemented with 10 nM BCDX2 (either GFP-BC plus DX2 or BC plus DX2-GFP, as indicated). Initially flushing the ssDNA curtains with the mCherry-RPA and BCDX2 containing buffer for 5 min at a flow rate of 0.8 mL/min. Then the valve was switched to the unlabeled RPA and BCDX2 containing buffer. Data were collected continuously throughout the entire process at a rate of 1 frame per 10 seconds.

Single-molecule data collection and analysis

For all two-color images, a custom-built shuttering system was used to avoid signal bleed-through during image acquisition [44]. Images from the green (GFP) and the red (mCherry) channels are recorded independently, generating an offset by 100 ms between the excitation of each color. This system prevents any possible signal bleed-through between the two channels. The lasers were shuttered between each acquired image to minimize photo-bleaching. Images were captured at an acquisition rate of 1 frame per 10 seconds for BCDX2 binding to RPA–ssDNA, or 1 frame per 3 seconds for RAD51 filament assembly in the presence of BCDX2 with a 100-millisecond integration time. Raw TIFF images were imported as image stacks into ImageJ, and kymographs were generated from the image stacks by defining a 1-pixel wide region of interest (ROI) along the long-axis of the individual ssDNA molecules. All data analysis was performed using the resulting kymographs.

For calculating BCDX2 binding kinetics to RPA-ssDNA, kymographs were generated by defining a 1–pixel–wide region of interest (ROI) along the length of individual ssDNA-filaments. Integrated signal intensity for each time point was obtained from individual kymographs and normalized using the maximum value for that kymograph. The mean and 95% CI of normalized intensities across all ssDNA molecules was plotted in Graphpad Prism (version 6.0) for each time point using XY connecting line curve. Experiments containing ATPγS or AMP-PNP were carried out under the same procedure.

For calculating assembly kinetics, kymographs were generated by defining a 1–pixel–wide region of interest (ROI) along the length of individual ssDNA–filaments. Integrated signal intensity for each time point was obtained from individual kymographs and normalized using the maximum value for that kymograph. The mean and 95% CI of normalized intensities across all ssDNA molecules was plotted for each time point, and the distribution was fit to a single exponential decay curve using GraphPad Prism (version 6.0) to obtain the rate constants. Experiments containing ATPγS were carried out under the same procedure.

Extended Data

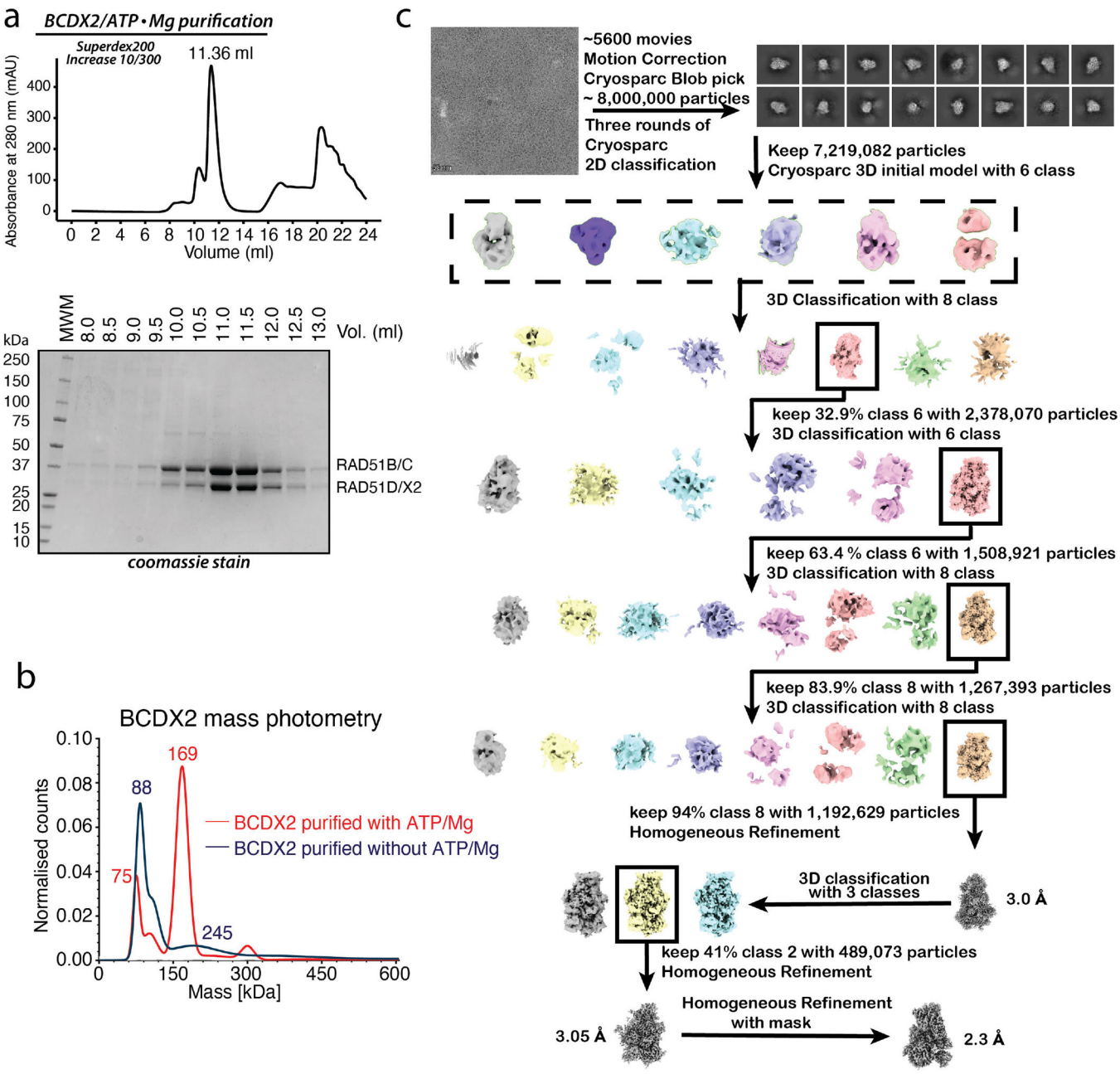

Extended Data Fig. 1 |. BCDX2 reconstitution and cryo-EM data processing flowchart for apo structure

a, Chromatogram of an analytical gel filtration of the BCDX2 complex in the presence of ATP/Mg on a Superdex200 Increase 10/300 column expressed and purified as described in the *Methods (top).* Coomassie-stained SDS-PAGE gel of the Indicated fractions *(bottom).* **b**, Mass photometry analysis of the BCDX2 complex purified in the presence (red) and absence (blue) of ATP/Mg. Both samples were rapidly diluted into PBS Immediately prior to data aquisition. **c**, Auto-picked particles were first sorted by three rounds of 2D classification, six

initial models were made first then followed by four rounds of heterogenous refinement. A final step of stringent heterogenous refinement and tight mask homogeneous refinement led to a final higher resolution map. All data analysis were performed using Cryosparc v3.3.1.

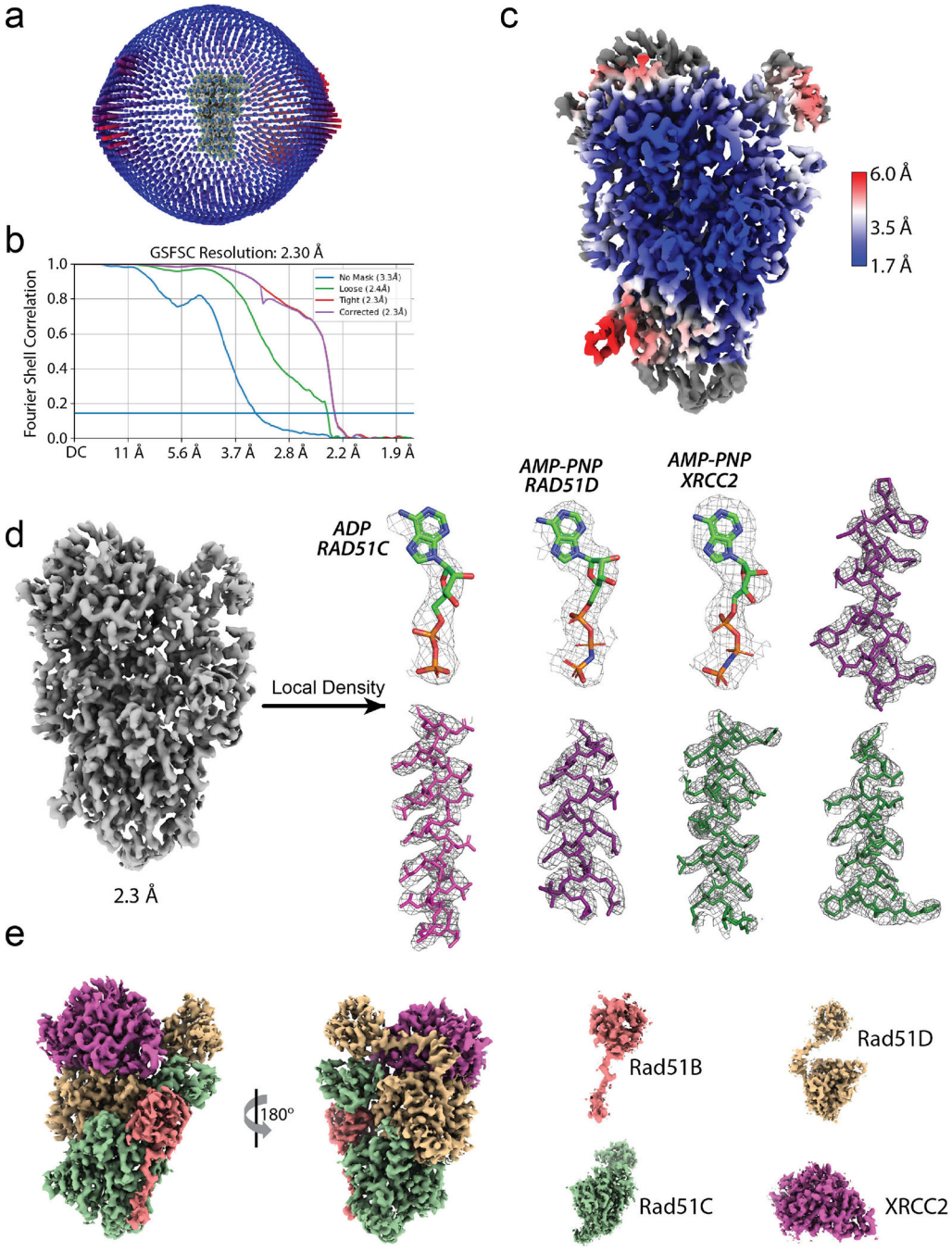

Extended Data Fig. 2 |. Quality of the apo BCDX2 complex cryo-EM reconstruction

a, The final Euler angle distribution of particles used for 3D refinement. **b**, Fourier Shell Correlation (FSC) plot from two half maps, with an overall resolution of 2.3 Å as determined at 0.143 criterion. **c**, Local resolution map color-coded from lower (red) to

higher resolution (blue). **d**, Overall map (left) and detailed views of local cryo-EM density for selected regions of the BCDX2 complex. **e**, Cryo-EM map of the BCDX2 complex with two views related by a 180° rotation about the y-axis (left). Maps of the individual subunits are shown in the right with Rad51B (pink), Rad51C (green), Rad51D (yellow), XRCC2 (purple).

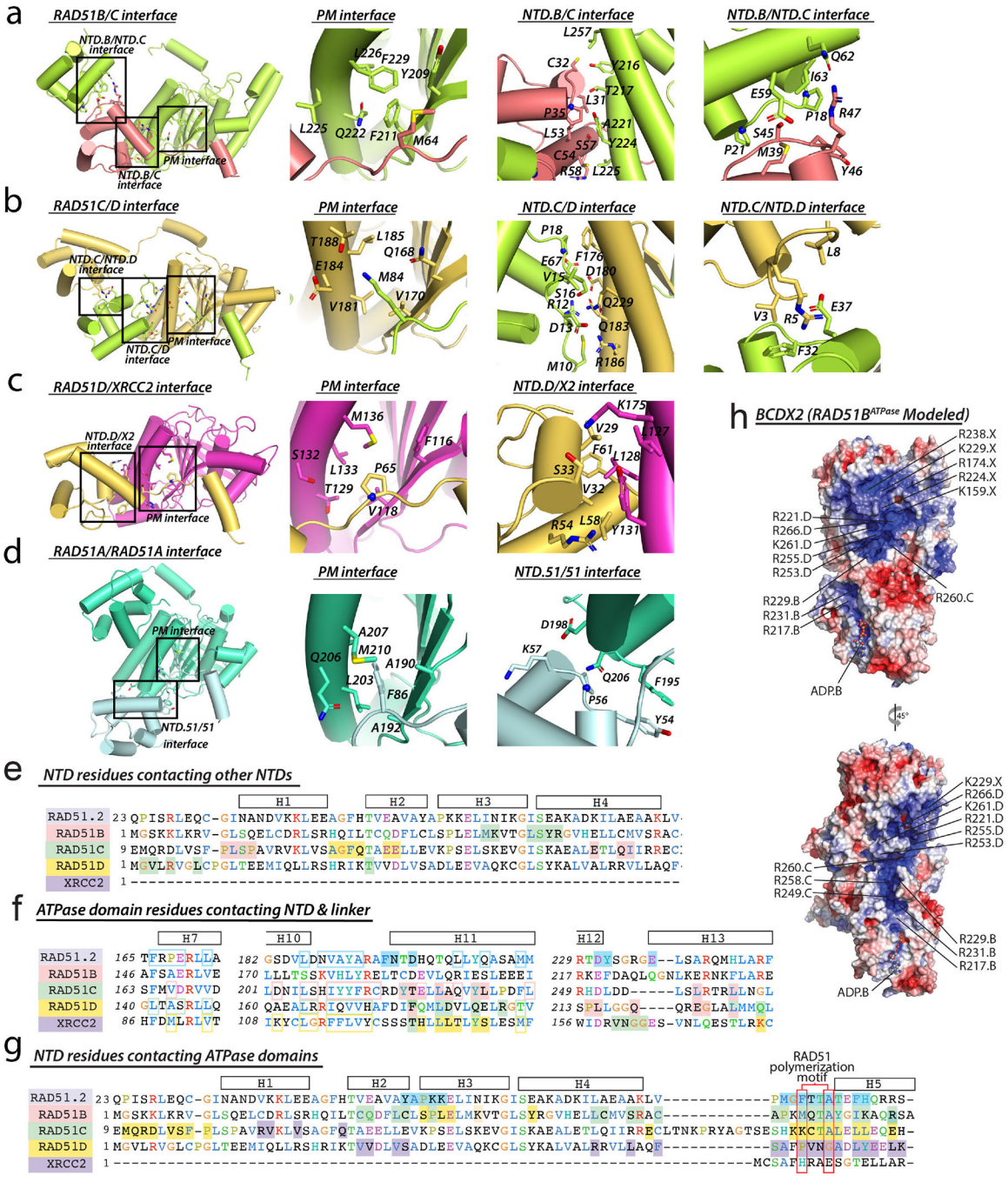

Extended Data Fig.3 |. Subunit-subunit interaction networks within the BCDX2 complex.

a, Cartoon representation of the indicated RAD51B/RAD51C interface with residues involved in intermolecular interaction shown as sticks. An overview of the complex is shown on the left with magnified views of the indicated interfaces presented in the three right panels, **b-d** The indicated complexes are presented as in panel *a* with RAD51C/RAD51D (panel *b),* RAD51D/XRCC2 (panel c), and RAD51/RAD51 from the presynaptic filament (PDB: 7EJC) (panel *d).* **e-g**, Structure-based sequence aligment of the indicated proteins. Residue numbers to the left of the sequence, secondary structure elements (RAD51 as a reference) are shown on top of the sequence. Contacts to RAD51 (shaded cyan), RAD51B (salmon), RAD51C (green), RAD51D (gold), and XRCC2 (magenta). In panel *g,* solid shade indicates ATPase domain contacts to the NTD and boxed shaded regions indicate contacts to the linker. **h**, Surface electrostic representation of the complete BCDX2 complex with the ATPase domain of RAD51B modeled using AlphaFold and residues comprising the basic patch which serves as the putative nucleic acid binding site labeled.

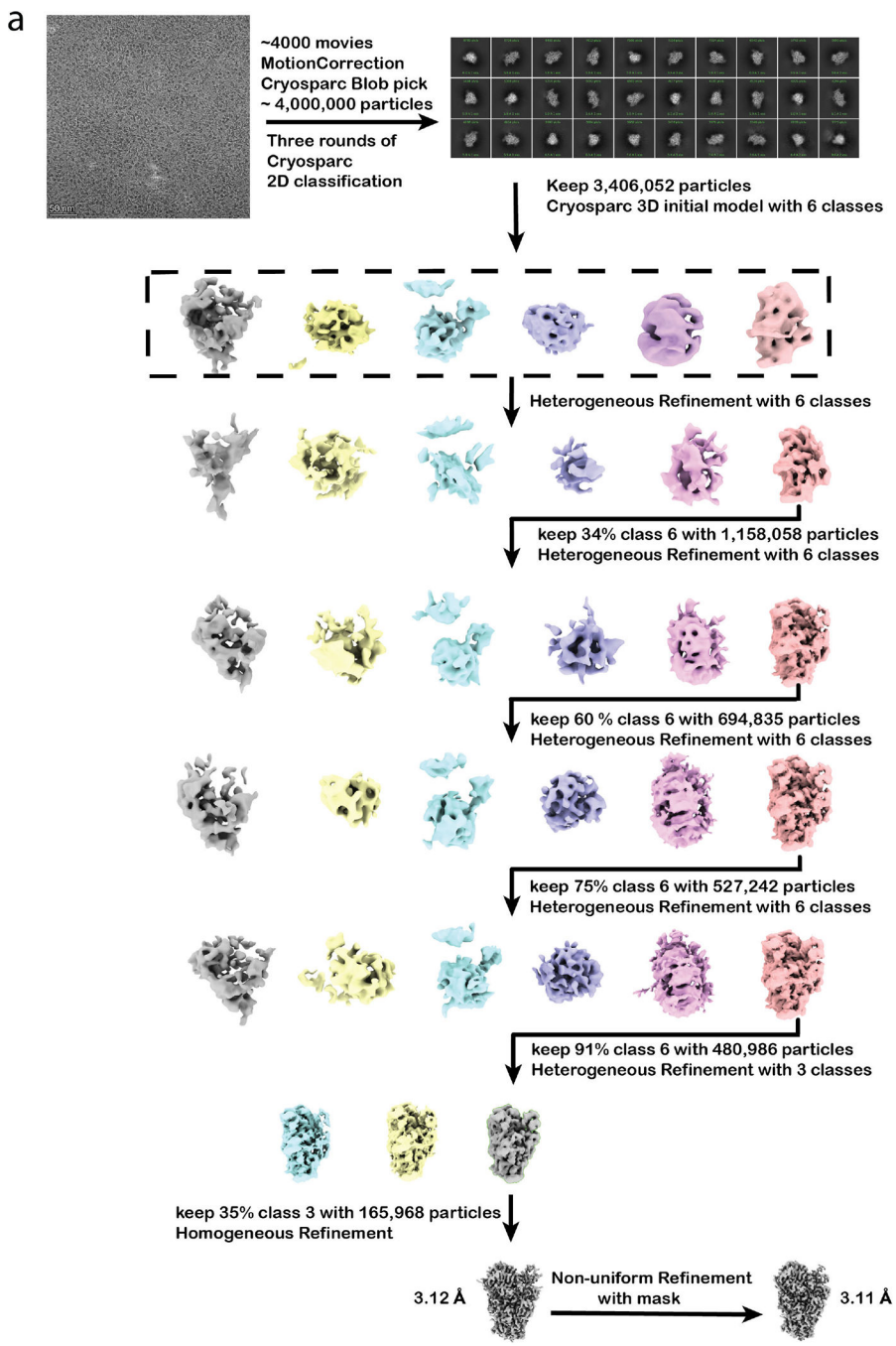

Extended Data Fig. 4 |. Cryo-EM data processing flowchart for the BCDX2/ssDNA structure

a, Auto-picked particles were first sorted by three rounds of 2D classification. Next, six initial models were generated, followed by four rounds of heterogenous refinement. A subsequent step of stringent heterogenous refinement and tight mask homogeneous refinement of class 3 resulted in a map with 3.12 Å resolution. A final non-uniform refinement yields final map of 3.11Å resolution. All data processing was performed using Cryosparc v3.3.1.

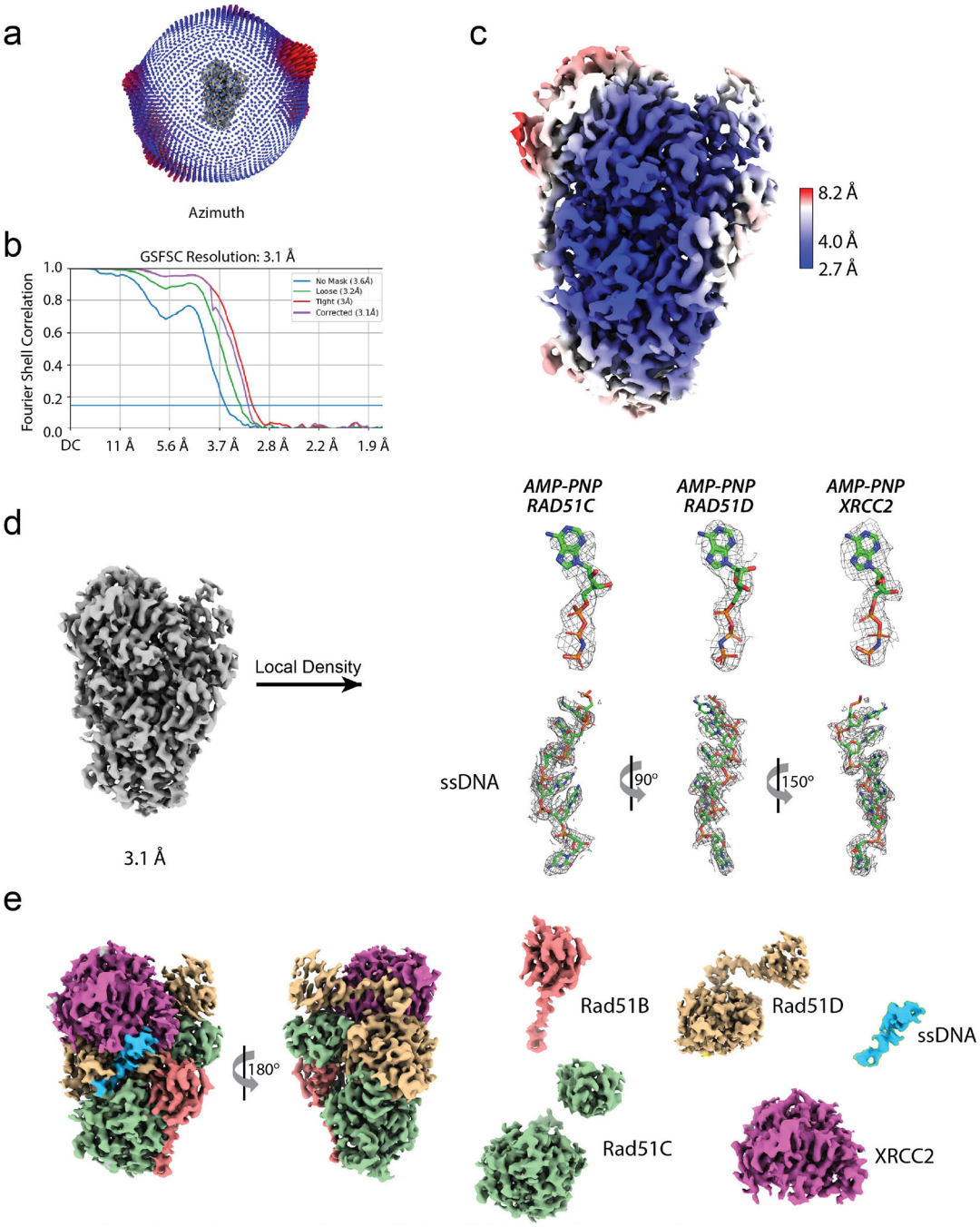

Extended Data Fig. 5 |. Quality of the BCDX2-ssDNA complex cryo-EM reconstruction

a, The final Euler angle distribution of particles used for 3D refinement. **b**, Fourier Shell Correlation (FSC) plot from two half maps, with an overall resolution of 3.1 Å as determined at 0.143 criterion. **c**, Local resolution map color-coded from lower (red) to higher resolution (blue). **d**, Overall map (left) and detailed views of local cryo-EM density for AMP-PNP and ssDNA from the BCDX2/ssDNA structure. **e**, Cryo-EM map of the BCDX2 complex with two views related by a 180° rotation about the y-axis (left). Maps of

the individual subunits are shown in the right with Rad51B (pink), Rad51C (green), Rad51D (yellow), XRCC2 (purple), ssDNA (cyan).

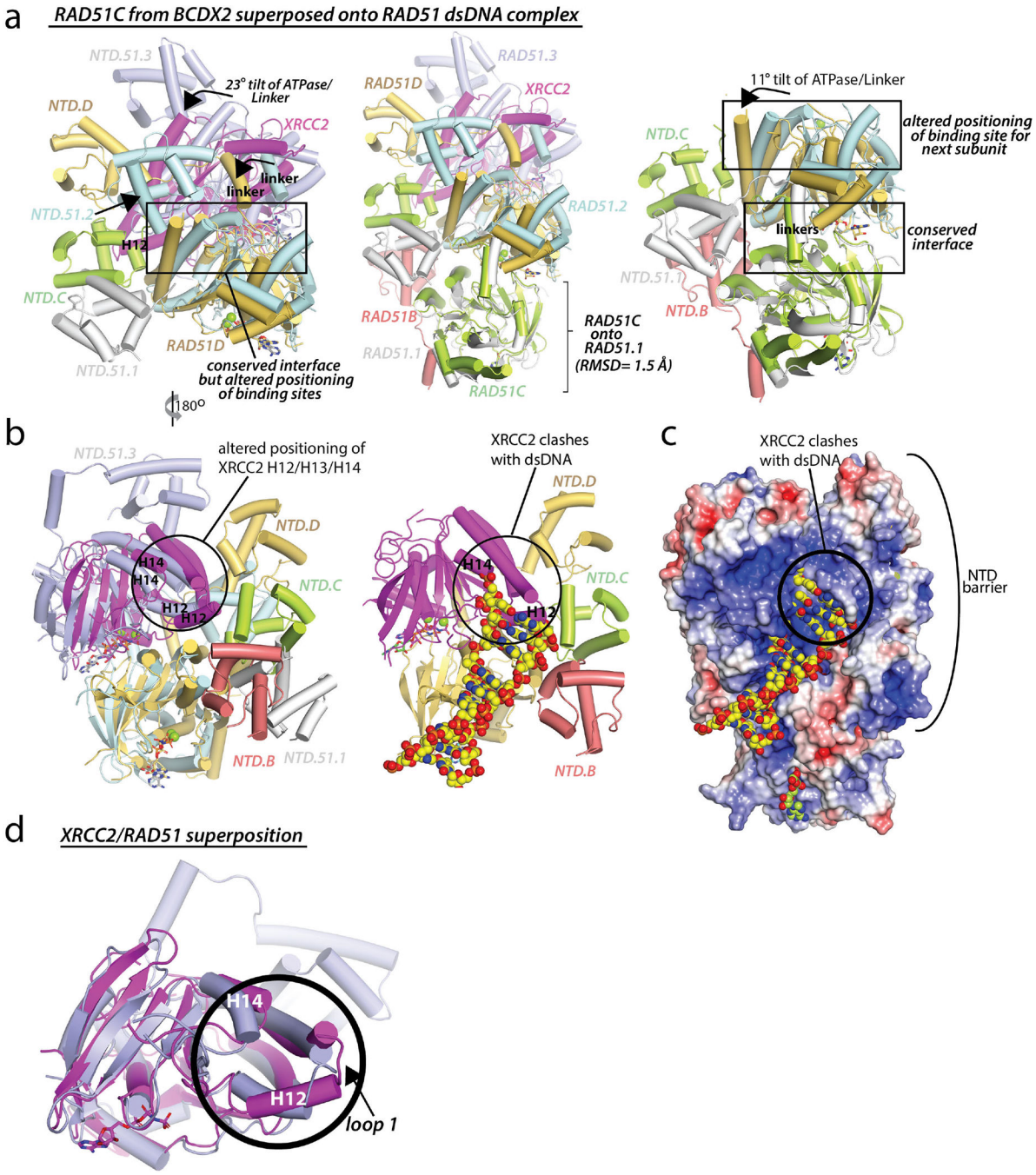

Extended Data Fig.6 |. A potential mechanism for the ssDNA binding specificity of BCDX2

a, RAD51C from BCDX2 was superposed onto RAD51 from the RAD51/ssDNA postsynaptic structure (PDB: 7EJE). Three subunits from the RAD51 filament are presented. An overview of the superposition is shown in the *center* panel, while magnified views of the RAD51C/RAD51D and RAD51D/XRCC2 subcomplexes are shown to the *right* and

left, respectively. **b**, Magnified view of the RAD51D/XRCC2 module from panel *a,* rotated 180 degrees about the y-axis *(left). Right,* dsDNA from the RAD51/dsDNA postsynaptic complex is shown as spheres with the RAD51 structure ommitted for clarity. Note clashes between dsDNA and XRCC2 due to 11 and 23 degree tilts at the RAD51C/RAD51D and RAD51D/XRCC2 interfaces, respectively, compared to RAD51. **c**, Surface electrostatic representation of the BCDX2 complex with dsDNA from the superposition presented in panels *a* and *b*. Note clashes between dsDNA and XRCC2 and close proxmity of the NTDs of BCDX2 to dsDNA. **d**, Superposition of XRCC2 onto RAD51. Note structural differences in length and conformation of the loop 1 region including helices H12 and H14, which clash with dsDNA in the model.

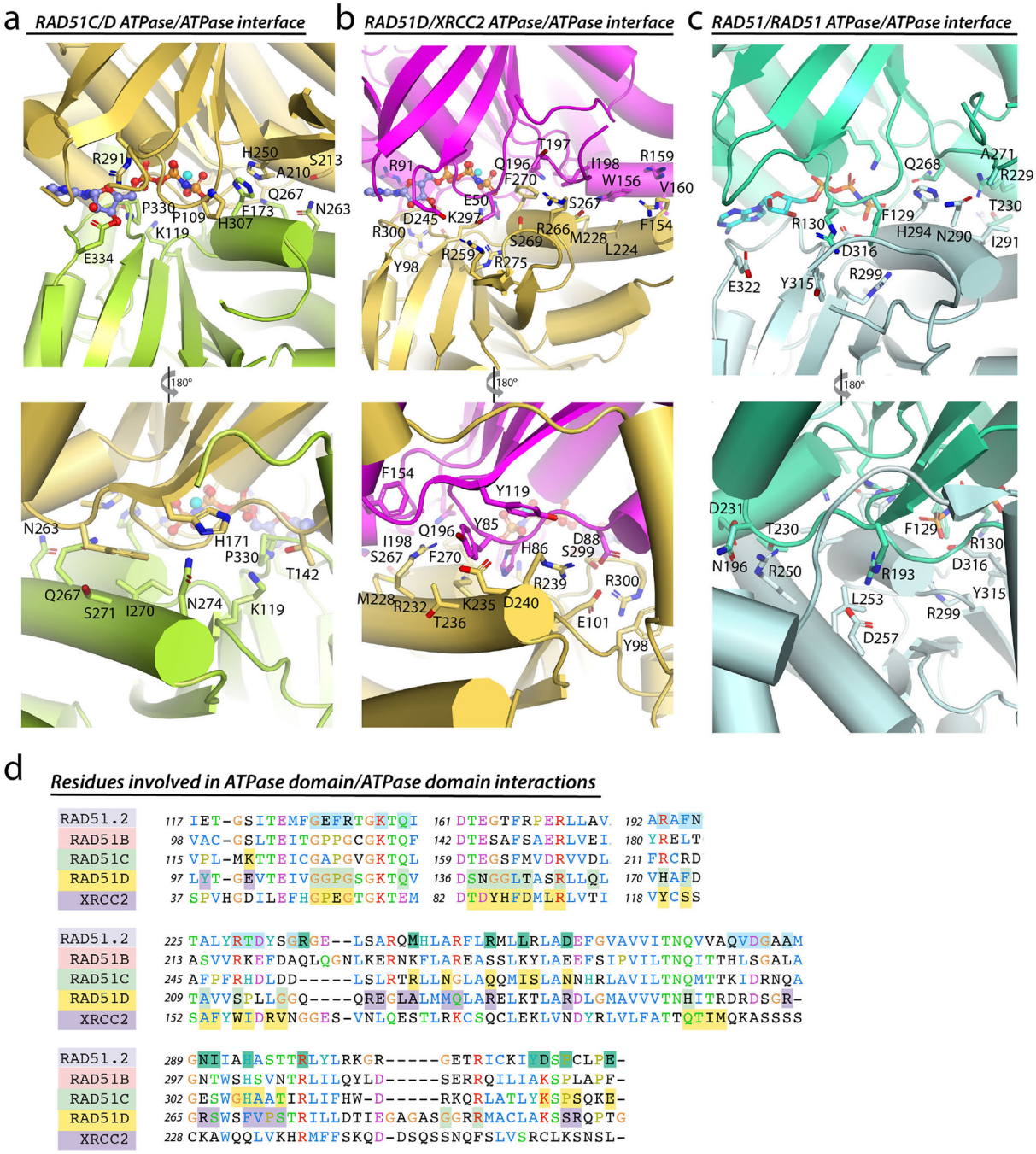

Extended Data Fig.7 |. Comparision of ATPase/ATPase domain interactions in BCDX2 and RAD51

a-c, Analysis of the amino acid interaction networks at the ATPase/ATPase interfaces of the RAD51C/RAD51D (**a**), and RAD51D/XRCC2 (**b**) subcomplexes of BCDX2, and RAD51/RAD51 from the RAD51/ssDNA presynaptic filament complex (PDB:7EJC) (**c**). Structures are shown as cartoon representations with residues involved in intermolecular interactions shown as sticks. Two views of the complexes related by a 180 degree rotation about the y-axis are shown in the top and bottom panels. **d**, Structure-based sequence alignment

highlighting ATPase domain/ATPase domain interactions at the interfaces higlighted in panels *a-c.* Residues are colored by the subunit to which they interact: RAD51C (green), RAD51D (gold), XRCC2 (magenta), and RAD51 (cyan). The ATPase domain of RAD51B is not visible in the BCDX2 structure but is included in the sequence alignment for comparison.

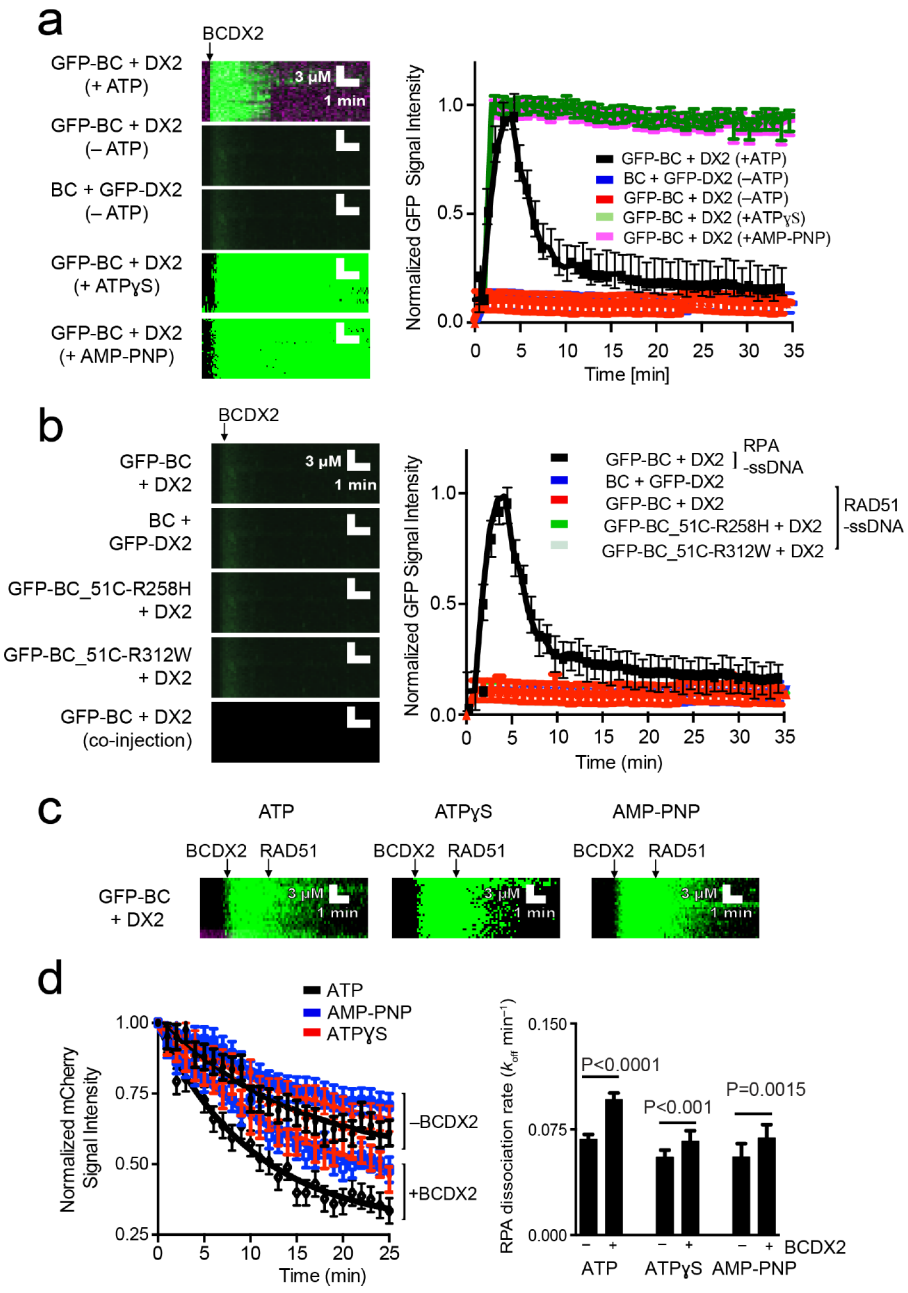

Extended Data Fig.8 |. Characterization of BCDX2 recombination mediatior activity

a, Representative kymographs of single ssDNA molecules *{left panel)* showing GFP-BC + DX2 plus ATP (reproduced from Fig. 6a, for comparison), GFP-BC + DX2 minus ATP, BC + GFP-DX2 minus ATP, GFP-BC + DX2 plus ATPγS and GFP-BC + DX2 (green channel;

10 nM each protein complex) plus AMP-PNP (2.5 mM ATP or ATP analogue) binding to mCherry-RPA-ssDNA (red channel). The graph *(right panel)* shows quantification of GFP-BCDX2 binding to the mCherry-RPA-ssDNA. The graph for GFP-BC + DX2 was reproduced from Fig. 6b for comparison. Data are represented as mean normalized GFP signal Intensity; error bars represent 95% Cl. Data were derived from three flow cells per reaction condition. **b**, Representative kymographs of single ssDNA molecules *(left panel)* showing GFP-BC + DX2 (reproduced from Fig. 6a, for comparison), GFP-BC-R258H + DX2, GFP-BC-R312W + DX2 (10 nM each protein complex) in the presence of 2.5 mM ATP binding to and dissociating from a mCherry-RPA-ssDNA. The graph *(right panel)* shows quantification of GFP-BCDX2 binding to the mCherry-RPA-ssDNA. The graph for GFP-BC + DX2 (+ATP) was reproduced from Fig. 6b for comparison. Data are represented as mean normalized GFP signal Intensity; error bars represent 95% Cl. Data were derived using three flow cells per reaction condition. **c**, Representative kymographs of single RPA-ssDNA molecules showing the behavior of GFP-BC+DX2 In reactions with ATP *(left kymograph),* ATPγS *(center kymograph)* and AMP-PNP *(right kymograph)* during RAD51 filament assembly. **d**, Quantification of mCherry-RPA dissociation during RAD51 filament assembly In the presence and absence of BCDX2 *(left panel),* as Indicated. Data represented the mean normalized mCherry signal Intensity. Data were derived using three flow cells per reaction condition. Calculated rates for RPA-mCherry dissociation from ssDNA during RAD51 filament assembly *(right panel).* Error bars represent 95% Cl.

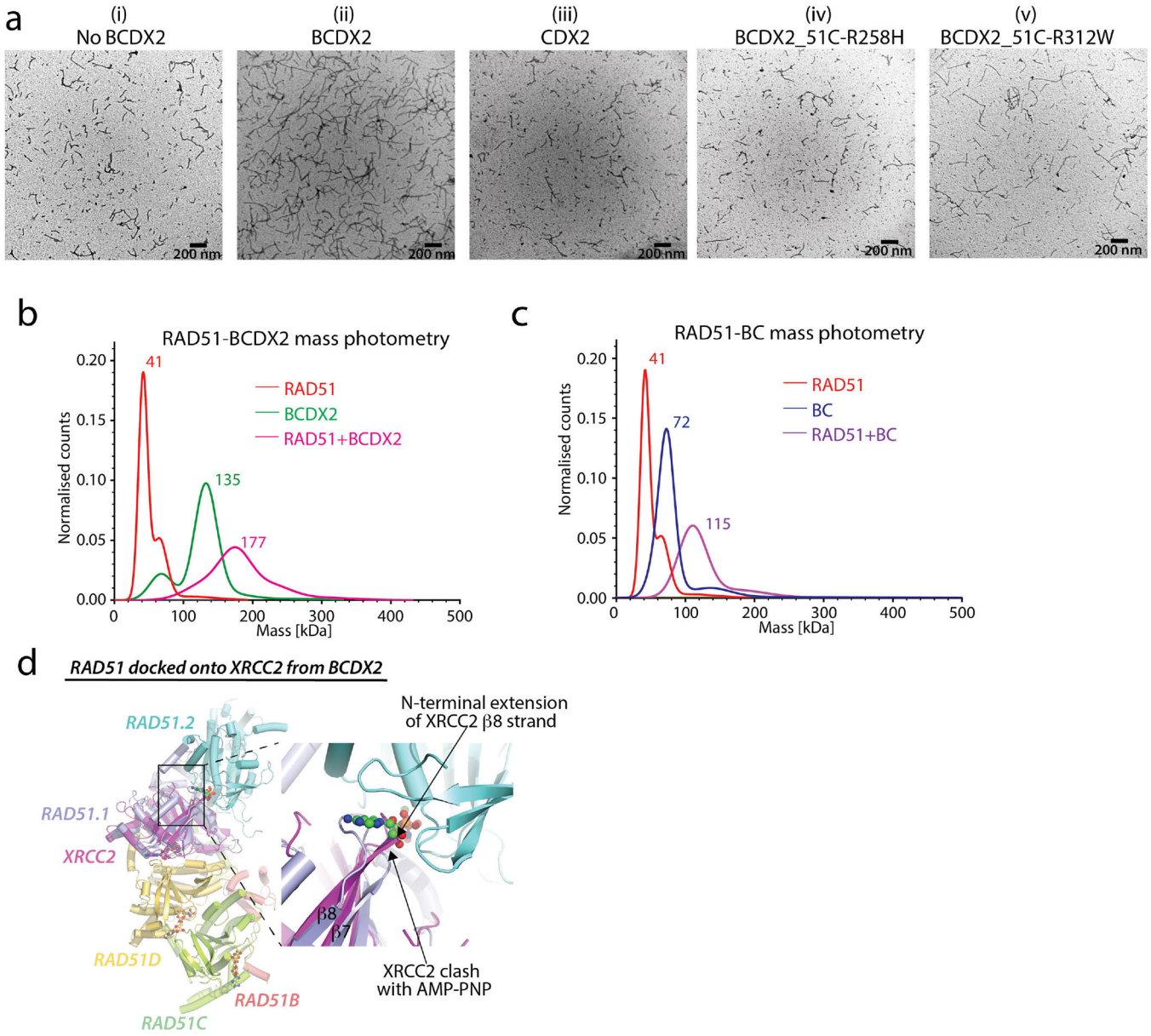

Extended Data Fig.9 |. Negative stain EM and BCDX2/RAD51 interactions

a, Representative micrographs depicting RAD51 nucleoprotein filaments seen by negative stain electron microscopy in absence or presence of BCDX2, CDX2 and BCDX2 with RAD51C mutants R258H and R312W. **b,c**, Mass photometry analysis of the RAD51 interactions with (**b**) BCDX2 complex and (**c**) BC sub-complex in the presence of ATP/Mg. Plots representing molecular mass profiles RAD51, BCDX2, BC alone alone and RAD51 when mixed with BCDX2 or BC are differently color coded and molecular mass of most prominent peak in each sample is indicated, **d**, A two protomer fragment of the RAD51 presynaptic filament (RAD51.1 in slate and RAD51.2 in cyan) were superimposed onto the XRCC2 subunit of XRCC2 subunit of the BCDX2 complex. The overall model is shown in the left panel and a magnified view of the ATP binding site at the interface between XRCC2 and RAD51.1 is shown in the left panel. Note that the β8 strand of XRCC2 is

extended by several residues and the loop between β7 and β8 adops a significantly different conformation from RAD51 which clashes with ATP in the model.

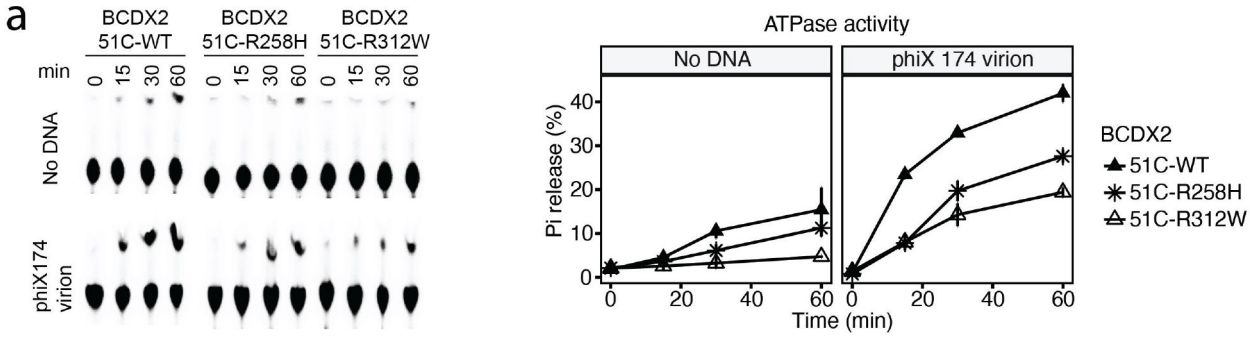

Extended Data Fig.10 |. ATPase analysis of cancer patient-derived BCDX2 subunit mutations

a, ATP hydrolysis with 1 μM WT and indicated mutant BCDX2 complexes with or without ssDNA were assessed for indicated time points and measurements for three independent experiments were plotted.

Extended Data Table 1 |

Cryo-EM data collection, refinement, and validation statistics

	BCDX2 complex	**BCDX2-ssDNA**
PDB ID	8FAZ	8GBJ
EMD ID	EMD-28961	EMD-29917
Voltage (kV)	200	200
Electron exposure (e–/Å^2)	51	52
Initial particle images	7,219,082	3,406,052
Final particle images	489,073	165,968
Symmetry imposed	C1	C1
Resolution, unmasked, FSC threshold 0.143 (Å)	3.3	3.6
Resolution, masked, FSC threshold 0.143 (Å)	2.3	3.1
Refinement Statistics		
Refinement program	Phenix, real space	Phenix, real space
Protein//ligand atoms/nucleotide(non-H)	7,280/91/0	7,468/93/118
RMSD bond (Å)	0.002	0.004
RMSD angles (°)	0.444	0.633
B-factors:protein/ligand/nucleotide (Å^2)	67.8/61.8	48.6/18.3/49.8
Ramachandran plot statistics (%)		
favored	97.6	97.6
allowed	2.4	2.4
Outliers	0	0
All-atom clash score		
MolProbity Score	1.6	1.7
Clashscore	10.4	14.6

Extended Data Table 2 |

Sequence and structural similarity between RAD51 and BCDX2 ATPase domains

Protein 1	Protein 2	Superposition Length	RMSD (Å)	% Identity	% Similarity
RAD51	RAD51C	218	1.49	29	43
RAD51	RAD51D	220	1.86	25	41
RAD51	XRCC2	225	2.68	21	34
RAD51C	RAD51D	214	2.05	23	41
RAD51C	XRCC2	221	3.06	20	33
RAD51D	XRCC2	220	2.59	16	36

Extended Data Table 3 |

Sequence and structural similarity between RAD51 and BCDX2 NTDs

Protein 1	Protein 2	Superposition Length	RMSD (Å)	% Identity	% Similarity
RAD51	RAD51C	57	1.74	25	40
RAD51	RAD51D	61	2.09	13	28
RAD51C	RAD51D	56	2.08	15	41

*XRCC2 lacks an NTD

Extended Data Table 4 |

SPR analysis of RAD51 and BCDX2 interaction

Analyte	Ligand	ka(1/Ms)	kd(1/s)	KD(M)
RAD51	BCDX2	3.09×10^{5}	7.91×10^{-4}	2.56×10^{-9}
RAD51	BC	3.23×10^{5}	2.78×10^{-4}	8.61×10^{-10}
RAD51	DX2	N/A	N/A	N/A

N/A: not available. The data could not be reasonably fit into a model

ka: association rate constant

kd: dissociation rate constant

KD: dissociation equilibrium constant

Note: Heterogeneous model was used for data fitting, and the tight binding stage was used as the interaction between the analyte and ligand listed.

Acknowledgements

The authors thank members of the Sung, Greene, and Olsen laboratories for discussions. Research reported in this publication was supported by NIH grants R01 GM115568 and R01 GM128731 (S.K.O.); R01 CA168635, R01 ES007061, P01 CA92584, R35 CA241801 (P.S.); R00 GM140264 (E.V.W); R01 CA221858 and R35 GM118026 (E.C.G.), R01 GM141091 and RSG-22-721675-01-DMC (W.Z.), R01 CA246807 and R01 CA258381 (S.B.), R01 GM136717, R01 CA237286, R01 CA188347, and Congressionally Directed Medical Research Programs BC191160 (A.V.M.), R50 CA265315 (Y.K.), R01 ES030335, ES031796 and the Department of Defense BC201356 (K.A.B.), and R01 CA139429 and Cancer Prevention and Research Institute of Texas RP220269 (R.H.). P.S. is the holder of the Robert A. Welch Distinguished Chair in Chemistry (AQ-0012) and the recipient of a CPRIT REI Award (RR180029). A.V.M. is the holder of the Joe R. and Teresa Lozano Long Chair in Cancer Research and is recipient of a CPRIT REI Award (RR210023). S.K.O. is the recipient of a CPRIT Rising Star Award (RR200030), and E.V.W. is the recipient of a CPRIT Recruitment of First Time Tenure Track Faculty Award (RR220068). E.C.G.

is a recipient of a Wellcome Trust Collaborative Award in Science (206292/D/17/Z). The cryo-EM data used for the BCDX2 reconstruction was collected at the UT Health San Antonio Cryo-EM Facility on a Glacios TEM equipped with a Falcon IV camera and Selectris energy filter purchased with the support of UT STARs awards 402–1288 (P.S) and 402–1317 (S.K.O.). We thank Axel Brilot for assistance screening cryo-EM grids at the University of Texas at Austin Sauer Structural Biology Laboratory (RRID:SCR_022951). We thank Barbara Hunter at the UTHSA Electron Microscopy Laboratory of South Texas Reference Laboratories, Department of Pathology and laboratory Medicine, for assistance with negative stain EM. The SPR assay was done in the Center for Innovative Drug Discovery and the Mays Cancer Center Drug Discovery and Structural Biology Shared Resource supported by CPRIT Core Facility Award RP160844 (D.Z.) and NIH-NCI P30 CA054174 (S.K.O. and D.Z.), respectively. The content of this study is solely the responsibility of the authors and does not necessarily represent the official views of the NIH.

Data Availability

Atomic coordinates for apo BCDX2 and BCDX2/ssDNA complexes are deposited in the RCSB with accession codes 8FAZ and 8GBJ, respectively. The corresponding cryo-EM maps have been deposited into the Electron Microscopy Data Bank with accession numbers EMD-28961 (apo BCDX2) and EMD-29917 (BCDX2/ssDNA). Extended data is available for this paper.

References

1. Sung P & Klein H Mechanism of homologous recombination: mediators and helicases take on regulatory functions. Nat Rev Mol Cell Biol 7, 739–750, doi:10.1038/nrm2008 (2006). [PubMed: 16926856]
2. Sullivan MR & Bernstein KA RAD-ical New Insights into RAD51 Regulation. Genes (Basel) 9, doi:10.3390/genes9120629 (2018).
3. Meindl A et al. Germline mutations in breast and ovarian cancer pedigrees establish RAD51C as a human cancer susceptibility gene. Nat Genet 42, 410–414, doi:10.1038/ng.569 (2010). [PubMed: 20400964]
4. Kondrashova O et al. Secondary Somatic Mutations Restoring. Cancer Discov 7, 984–998, doi:10.1158/2159-8290.CD-17-0419 (2017). [PubMed: 28588062]
5. Garcin EB et al. Differential Requirements for the RAD51 Paralogs in Genome Repair and Maintenance in Human Cells. PLoS Genet 15, e1008355, doi:10.1371/journal.pgen.1008355 (2019). [PubMed: 31584931]
6. Prakash R et al. Homologous recombination-deficient mutation cluster in tumor suppressor. Proc Natl Acad Sci U S A 119, e2202727119, doi:10.1073/pnas.2202727119 (2022). [PubMed: 36099300]
7. Clarke TL & Mostoslavsky R DNA repair as a shared hallmark in cancer and ageing. Mol Oncol 16, 3352–3379, doi:10.1002/1878-0261.13285 (2022). [PubMed: 35834102]
8. Prakash R, Zhang Y, Feng W & Jasin M Homologous recombination and human health: the roles of BRCA1, BRCA2, and associated proteins. Cold Spring Harb Perspect Biol 7, a016600, doi:10.1101/cshperspect.a016600 (2015). [PubMed: 25833843]
9. Sigurdsson S, Trujillo K, Song B, Stratton S & Sung P Basis for avid homologous DNA strand exchange by human Rad51 and RPA. J Biol Chem 276, 8798–8806, doi:10.1074/jbc.M010011200 (2001). [PubMed: 11124265]
10. Zhao W et al. Promotion of BRCA2-Dependent Homologous Recombination by DSS1 via RPA Targeting and DNA Mimicry. Mol Cell 59, 176–187, doi:10.1016/j.molcel.2015.05.032 (2015). [PubMed: 26145171]
11. Masson JY et al. Identification and purification of two distinct complexes containing the five RAD51 paralogs. Genes Dev 15, 3296–3307, doi:10.1101/gad.947001 (2001). [PubMed: 11751635]
12. Martino J et al. The human Shu complex functions with PDS5B and SPIDR to promote homologous recombination. Nucleic Acids Res 47, 10151–10165, doi:10.1093/nar/gkz738 (2019). [PubMed: 31665741]

13. Yonetani Y et al. Differential and collaborative actions of Rad51 paralog proteins in cellular response to DNA damage. Nucleic Acids Res 33, 4544–4552, doi:10.1093/nar/gki766 (2005). [PubMed: 16093548]
14. Nalepa G & Clapp DW Fanconi anaemia and cancer: an intricate relationship. Nat Rev Cancer 18, 168–185, doi:10.1038/nrc.2017.116 (2018). [PubMed: 29376519]
15. Jacquinet A et al. Expanding the FANCO/RAD51C associated phenotype: Cleft lip and palate and lobar holoprosencephaly, two rare findings in Fanconi anemia. Eur J Med Genet 61, 257–261, doi:10.1016/j.ejmg.2017.12.011 (2018). [PubMed: 29278735]
16. Vaz F et al. Mutation of the RAD51C gene in a Fanconi anemia-like disorder. Nat Genet 42, 406–409, doi:10.1038/ng.570 (2010). [PubMed: 20400963]
17. Shamseldin HE, Elfaki M & Alkuraya FS Exome sequencing reveals a novel Fanconi group defined by XRCC2 mutation. J Med Genet 49, 184–186, doi:10.1136/jmedgenet-2011-100585 (2012). [PubMed: 22232082]
18. Miller KA, Sawicka D, Barsky D & Albala JS Domain mapping of the Rad51 paralog protein complexes. Nucleic Acids Res 32, 169–178, doi:10.1093/nar/gkg925 (2004). [PubMed: 14704354]
19. Xu J et al. Mechanisms of distinctive mismatch tolerance between Rad51 and Dmc1 in homologous recombination. Nucleic Acids Res 49, 13135–13149, doi:10.1093/nar/gkab1141 (2021). [PubMed: 34871438]
20. Pellegrini L et al. Insights into DNA recombination from the structure of a RAD51-BRCA2 complex. Nature 420, 287–293, doi:10.1038/nature01230 (2002). [PubMed: 12442171]
21. Rajendra E & Venkitaraman AR Two modules in the BRC repeats of BRCA2 mediate structural and functional interactions with the RAD51 recombinase. Nucleic Acids Res 38, 82–96, doi:10.1093/nar/gkp873 (2010). [PubMed: 19875419]
22. Yu DS et al. Dynamic control of Rad51 recombinase by self-association and interaction with BRCA2. Mol Cell 12, 1029–1041, doi:10.1016/s1097-2765(03)00394-0 (2003). [PubMed: 14580352]
23. Short JM et al. High-resolution structure of the presynaptic RAD51 filament on single-stranded DNA by electron cryo-microscopy. Nucleic Acids Res 44, 9017–9030, doi:10.1093/nar/gkw783 (2016). [PubMed: 27596592]
24. Xu J et al. Cryo-EM structures of human RAD51 recombinase filaments during catalysis of DNA-strand exchange. Nat Struct Mol Biol 24, 40–46, doi:10.1038/nsmb.3336 (2017). [PubMed: 27941862]
25. Chi P, Van Komen S, Sehorn MG, Sigurdsson S & Sung P Roles of ATP binding and ATP hydrolysis in human Rad51 recombinase function. DNA Repair (Amst) 5, 381–391, doi:10.1016/j.dnarep.2005.11.005 (2006). [PubMed: 16388992]
26. Sullivan MR et al. Long-term survival of an ovarian cancer patient harboring a RAD51C missense mutation. Cold Spring Harb Mol Case Stud 7, doi:10.1101/mcs.a006083 (2021).
27. Matsuo Y, Sakane I, Takizawa Y, Takahashi M & Kurumizaka H Roles of the human Rad51 L1 and L2 loops in DNA binding. FEBS J 273, 3148–3159, doi:10.1111/j.1742-4658.2006.05323.x (2006). [PubMed: 16780572]
28. Yang H, Zhou C, Dhar A & Pavletich NP Mechanism of strand exchange from RecA-DNA synaptic and D-loop structures. Nature 586, 801–806, doi:10.1038/s41586-020-2820-9 (2020). [PubMed: 33057191]
29. Gibb B, Silverstein TD, Finkelstein IJ & Greene EC Single-stranded DNA curtains for real-time single-molecule visualization of protein-nucleic acid interactions. Anal Chem 84, 7607–7612, doi:10.1021/ac302117z (2012). [PubMed: 22950646]
30. Gibb B et al. Concentration-dependent exchange of replication protein A on single-stranded DNA revealed by single-molecule imaging. PLoS One 9, e87922, doi:10.1371/journal.pone.0087922 (2014). [PubMed: 24498402]
31. Ma CJ, Gibb B, Kwon Y, Sung P & Greene EC Protein dynamics of human RPA and RAD51 on ssDNA during assembly and disassembly of the RAD51 filament. Nucleic Acids Res 45, 749–761, doi:10.1093/nar/gkw1125 (2017). [PubMed: 27903895]

32. Ma CJ, Steinfeld JB & Greene EC Single-Stranded DNA Curtains for Studying Homologous Recombination. Methods Enzymol 582, 193–219, doi:10.1016/bs.mie.2016.08.005 (2017). [PubMed: 28062035]
33. Jumper J et al. Highly accurate protein structure prediction with AlphaFold. Nature 596, 583–589, doi:10.1038/s41586-021-03819-2 (2021). [PubMed: 34265844]
34. Gayarre J et al. Characterisation of the novel deleterious RAD51C p.Arg312Trp variant and prioritisation criteria for functional analysis of RAD51C missense changes. Br J Cancer 117, 1048–1062, doi:10.1038/bjc.2017.286 (2017). [PubMed: 28829762]
35. Belan O et al. Single-molecule analysis reveals cooperative stimulation of Rad51 filament nucleation and growth by mediator proteins. Mol Cell 81, 1058–1073 e1057, doi:10.1016/j.molcel.2020.12.020 (2021). [PubMed: 33421363]
36. Roy U et al. The Rad51 paralog complex Rad55-Rad57 acts as a molecular chaperone during homologous recombination. Mol Cell 81, 1043–1057 e1048, doi:10.1016/j.molcel.2020.12.019 (2021). [PubMed: 33421364]
37. Špírek M, Taylor MRG, Belan O, Boulton SJ & Krejci L Nucleotide proofreading functions by nematode RAD51 paralogs facilitate optimal RAD51 filament function. Nat Commun 12, 5545, doi:10.1038/s41467-021-25830-x (2021). [PubMed: 34545070]
38. Punjani A, Rubinstein JL, Fleet DJ & Brubaker MA cryoSPARC: algorithms for rapid unsupervised cryo-EM structure determination. Nat Methods 14, 290–296, doi:10.1038/nmeth.4169 (2017). [PubMed: 28165473]
39. Pettersen EF et al. UCSF ChimeraX: Structure visualization for researchers, educators, and developers. Protein Sci 30, 70–82, doi:10.1002/pro.3943 (2021). [PubMed: 32881101]
40. Emsley P & Cowtan K Coot: model-building tools for molecular graphics. Acta Crystallogr D Biol Crystallogr 60, 2126–2132, doi:10.1107/S0907444904019158 (2004). [PubMed: 15572765]
41. Liebschner D et al. Macromolecular structure determination using X-rays, neutrons and electrons: recent developments in Phenix. Acta Crystallogr D Struct Biol 75, 861–877, doi:10.1107/S2059798319011471 (2019). [PubMed: 31588918]
42. Delano W The PyMOL molecular graphics system. DeLano Scientific, San Carlos CA, USA. http://www.pymol.org. (2002).
43. Gaines WA et al. Promotion of presynaptic filament assembly by the ensemble of S. cerevisiae Rad51 paralogues with Rad52. Nat Commun 6, 7834, doi:10.1038/ncomms8834 (2015). [PubMed: 26215801]
44. De Tullio L, Kaniecki K & Greene EC Single-Stranded DNA Curtains for Studying the Srs2 Helicase Using Total Internal Reflection Fluorescence Microscopy. Methods Enzymol 600, 407–437, doi:10.1016/bs.mie.2017.12.004 (2018). [PubMed: 29458768]
45. Greene EC, Wind S, Fazio T, Gorman J & Visnapuu ML DNA curtains for high-throughput single-molecule optical imaging. Methods Enzymol 472, 293–315, doi:10.1016/S0076-6879(10)72006–1 (2010). [PubMed: 20580969]
46. Roy U & Greene EC Single-Stranded DNA Curtains for Single-Molecule Visualization of Rad51-ssDNA Filament Dynamics. Methods Mol Biol 2281, 193–207, doi:10.1007/978-1-0716-1290-3_11 (2021). [PubMed: 33847959]

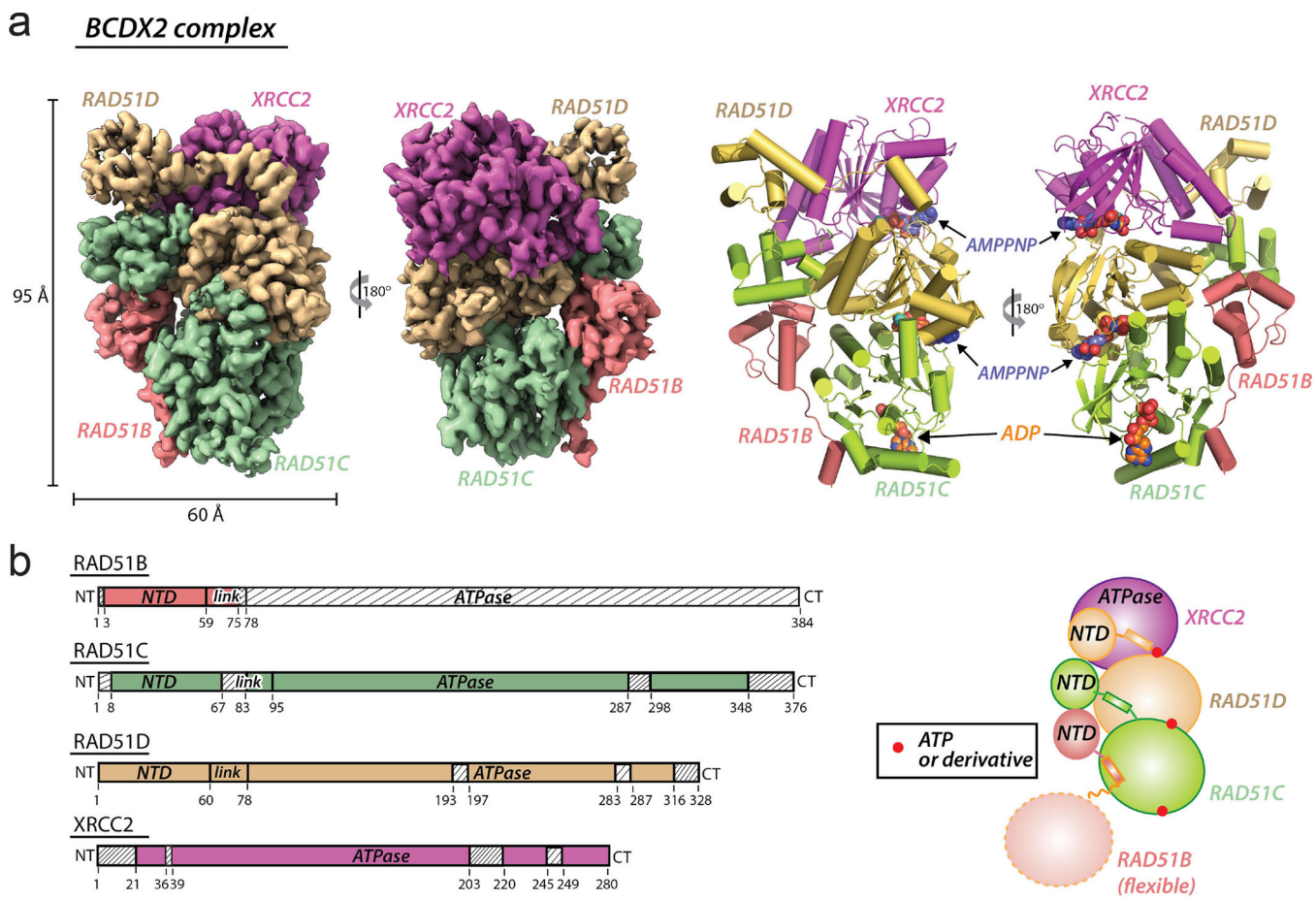

Fig. 1 |. Cryo-EM structure of the RAD51B/RAD51C/RAD51D/XRCC2 complex

a, Cryo-EM maps of the BCDX2 complex assembled in the presence of AMP-PNP (*left*). Individual subunits are labeled and color coded. Two views related by a 180 degree rotation about the y-axis are presented. Cartoon representation of the BCDX2 complex (*right*). ADP and AMP-PNP molecules are shown as spheres. b, Schematic outlining the domain organization of BCDX2 subunits with regions of disorder in the structure indicated by hatched boxes. A cartoon diagram highlighting the major structural features of the BCDX2 complex is shown to the *right.*

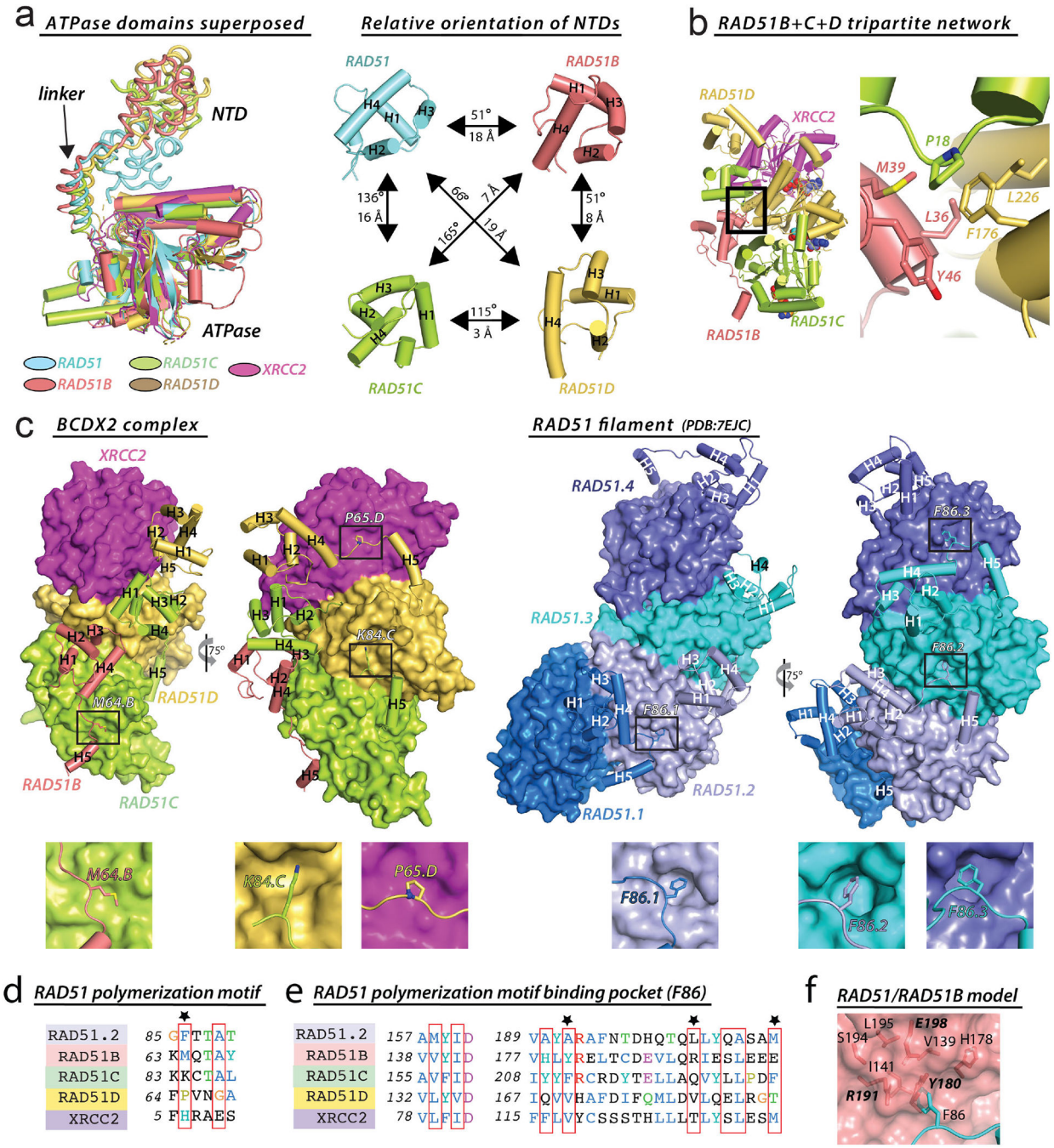

Fig. 2 |. BCDX2 architecture is reinforced by a unique NTD configuration

a, Relative orientation of NTD/linkers and ATPase domains of BCDX2 subunits. The ATPase domains of RAD51 and BCDX2 subunits superimposed and shown as cartoon representations colored as indicated (*left*). Linker and NTDs are shown as worms. Standalone NTDs with the relative rotation/translation between NTD pairs are shown in the *right* panel. **b**, A unique tripartite interaction between the NTDs of RAD51B and RAD51C and the ATPase domain of RAD51D. An overview of the structure is shown as cartoon representation in the *left* panel along with a magnified view of the tripartite network with

interacting residues shown as sticks is shown in the *right* panel. **c**, ATPase domains of the BCDX2 complex (*left*) and RAD51 filament (*right*) are shown as surface representations and linker/NTDs are shown as cartoons. Residues corresponding to the polymerization motif of RAD51 are shown as sticks, with magnified views shown on the *bottom*. The four different subunits of RAD51 are distinguished by numbers 1–4 appended to the labels (RAD51.1, RAD51.2, etc..). **d**, Structure-based sequence alignment of the RAD51 polymerization motif (PM). **e**, Structure-based sequence alignment of the RAD51 PM binding pocket. **f**, Model of RAD51/RAD51B showing the PM pocket of RAD51B filled by bulky hydrophobic and charged residues incompatible with Phe86 binding. RAD51B is shown as a semitransparent surface (salmon) with residues corresponding to the RAD51 PM binding pocket shown as sticks. Phe86 of the RAD51 PM is shown as sticks.

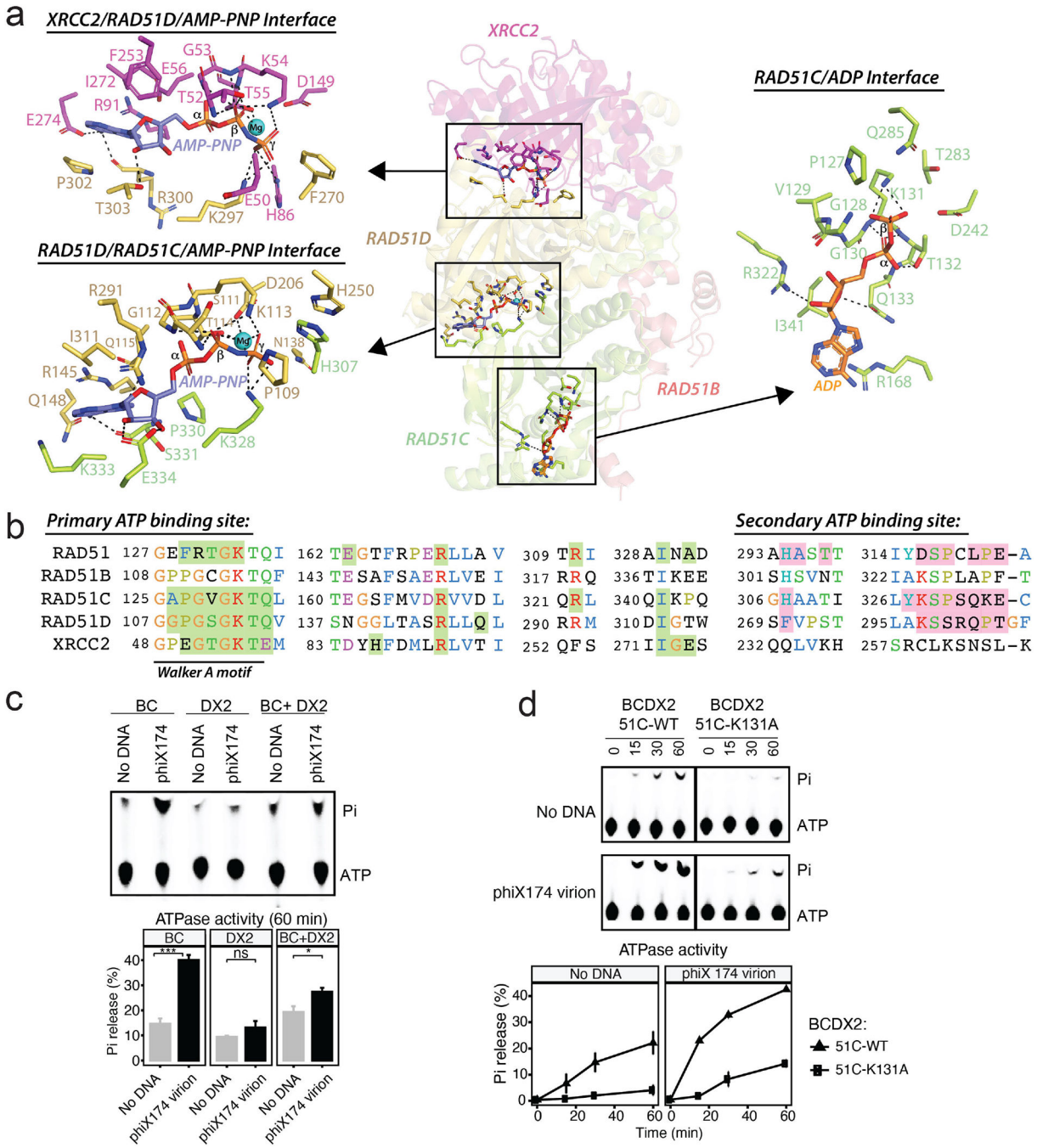

Fig. 3 |. Structural features and functional analysis of BCDX2 subunit active sites

a, Overview of the BCDX2 structure shown as a semitransparent cartoon with. ATP and BCDX2 residues contacting ATP are shown as solid sticks (*center*). Active sites are boxed. Magnified views of BCDX2 active sites are shown in the left and right panels. **b**, Structure-based sequence alignment of ATP binding sites of BCDX2 subunits and RAD51. Nucleotides are buried at the interface between subunits and the primary ATP binding site is defined as the subunit with its Walker A motif contacting ATP while the secondary ATP binding site is defined as the subunit contributing interacting residues on the other side of

ATP. Interacting residues from primary and secondary ATP binding sites are colored green and pink, respectively. RAD51 (PDB: 7EJC) is shown for reference. **c**, ATPase assays of the indicated BCDX2 variants in the presence or absence of ssDNA. Pi indicates released inorganic phosphate after hydrolysis. The histograms show results from three independent experiments and *p*-values for the significance of differences in mean values were calculated by the t.test are indicated as follows: ****, ≤ 0.0001; ***, ≤ 0.001; **, ≤ 0.01; *, ≤ 0.05; ns, > 0.05. **d.** ATP hydrolysis with 1μM WT and indicated mutant BCDX2 complexes with or without ssDNA were assessed for indicated time points and measurements for three independent experiments were plotted.

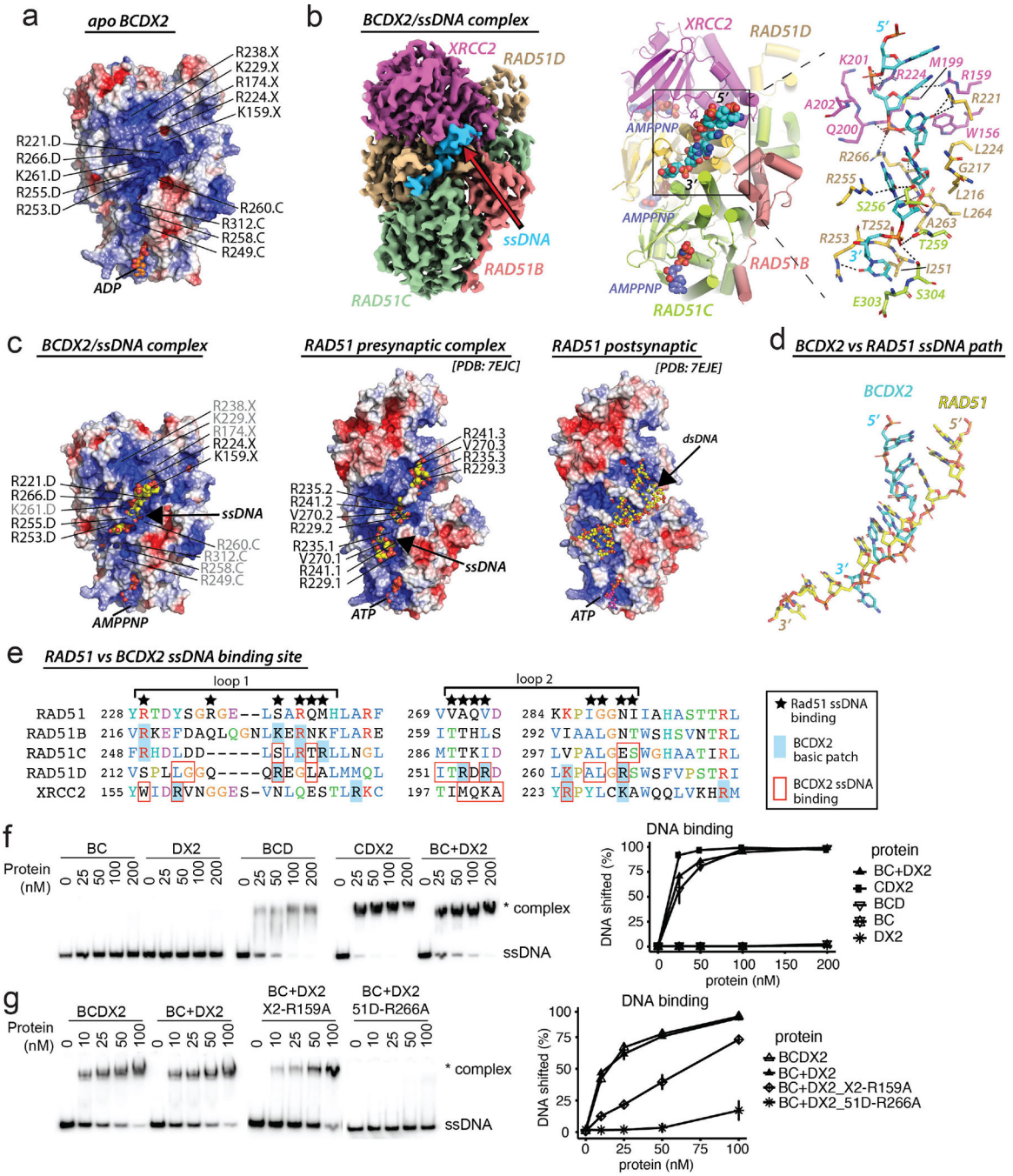

Fig. 4 |. Structural and functional analysis of the BCDX2 ssDNA binding site

a, Surface electrostatic representation of apo BCDX2 with residues comprising a highly basic surface labeled. **b**, Cryo-EM map of the BCDX2/ssDNA complex (*left*). Cartoon representation of the BCDX2/ssDNA complex (*center*). Magnified view of the BCDX2/ssDNA interface with ssDNA and ssDNA-interacting residues of BCDX2 shown as sticks (*right*). **c**, Surface electrostatic representations of the indicated complexes with ssDNA shown as spheres. ssDNA-interacting residues labeled with black text, residues from the BCDX2 basic patch not directly contacting ssDNA labeled with gray text. Subunit identity

for the BCDX2 complex is appended to the amino acid label (e.g. R255 of RAD51D as R255.D). **d**, ssDNA from BCDX2 and RAD51-bound complexes shown as sticks in the same view as *panel c*. **e**, Structure-based sequence alignment of RAD51 and BCDX2 ssDNA binding sites. Residues are labeled as indicated in the legend on the right. **f**, ssDNA binding by the BCDX2 subcomplexes at indicated concentrations was assessed by electrophoretic mobility shift assays using an 80-mer substrate. The graph shows results from three independent experiments. **g**, ssDNA binding by the BCDX2 comparing WT and DNA binding mutants in RAD51D or XRCC2 were analyzed as in *panel f* at the indicated protein concentrations.

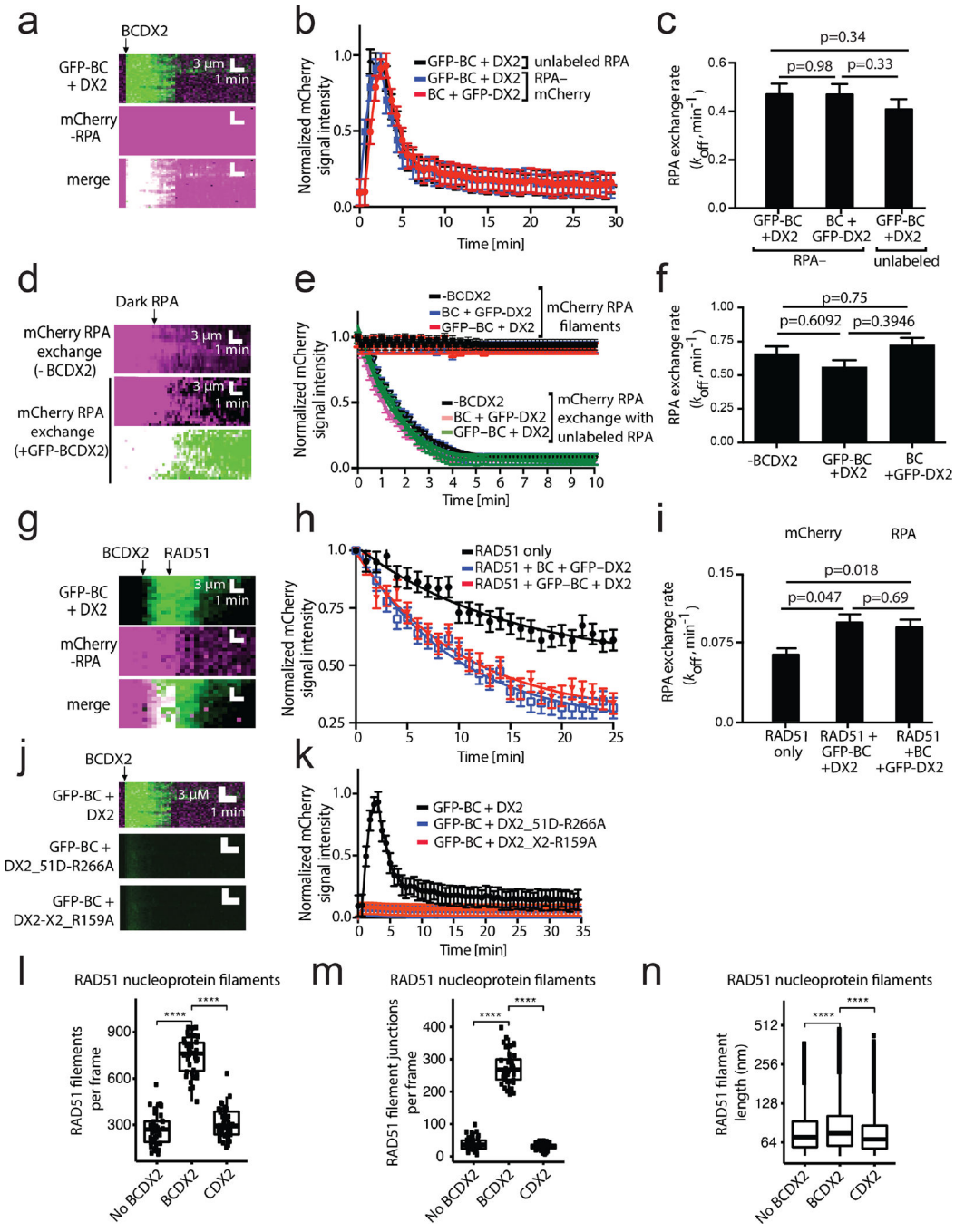

Fig. 5 |. Characterization of BCDX2 recombination mediator activity

a, Kymographs of a single ssDNA molecule showing GFP-BC + DX2 (10 nM each; green) binding and dissociating from mCherry-RPA-ssDNA (magenta) with 2.5 mM ATP. **b**, Normalized GFP signal intensities for GFP-BC + DX2 or BC + GFP-DX2 on RPA-ssDNA (unlabeled or mCherry-tagged, as indicated) with 2.5 mM ATP; for all experiments error bars represent 95% confidence intervals (CI). **c**, Rates of BCDX2 dissociation from RPA-ssDNA. **d**, Representative kymographs showing mCherry-RPA exchange with unlabeled RPA without BCDX2 or with GFP-BCDX2 (10 nM each; merged). **e**, Quantification

of mCherry RPA signal under the indicated conditions (with and without mCherry-RPA exchange). Data are represented as mean normalized mCherry signal intensity. **f**, Rates of mCherry-RPA exchange with unlabeled RPA with and without 10 nM BCDX2. **g**, Representative kymographs showing GFP-BC + DX2 (10 nM each; green) binding to mCherry-RPA-ssDNA (magenta) followed by injection of 500 nM Rad51 + 2.5 mM ATP. **h**, Quantification mCherry-RPA dissociation during RAD51 filament assembly with or without BCDX2. Data represented the mean normalized mCherry signal intensity. **i**, Rates of RPA-mCherry dissociation from ssDNA during RAD51 filament assembly. **j-k**, Representative kymographs of single ssDNA molecules (**j**) showing the indicated GFP-BCDX2 variant (10 nM each protein complex) in the presence of 2.5 mM ATP binding to and dissociating from a mCherry-RPA-ssDNA. The graph (**k**) shows quantification of GFP-BCDX2 binding to the mCherry-RPA-ssDNA. The kymograph and graph for GFP-BC + DX2 (+ATP) were reproduced from Figs. 5a and b, for comparison. Data are represented as mean normalized GFP signal intensity; error bars represent 95% CI. Data were derived using three flow cells per reaction condition. **l-m-n**, Box plots depict (**l**) number of RAD51 nucleoprotein filaments per frame, (**m**) number of junctions formed by filaments per frame and (**n**) length of filaments in nanometers measured by negative stain electron microscopy in absence or presence of BCDX2 and CDX2. The *p*-values for the significance of differences in median values were calculated by the Mann-Whitney-Wilcoxon test.

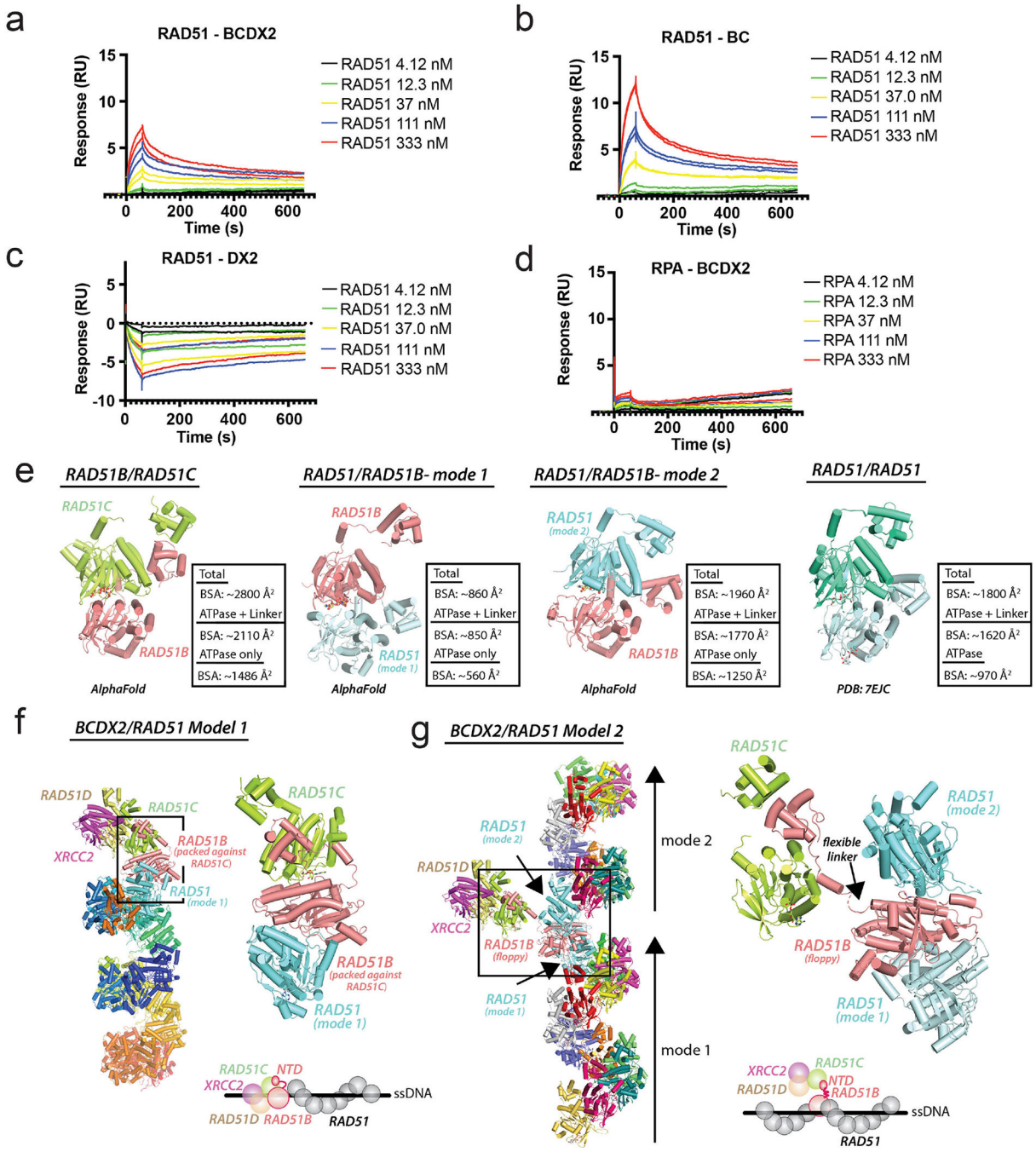

Fig. 6 |. SPR analysis and AlphaFold modeling of BCDX2/RAD51 interactions

a-c, Sensorgram from SPR experiments of RAD51 binding to (**a**) BCDX2, (**b**) BC, and (**c**) DX2. **d**, Sensorogram from SPR experiments of RPA binding to BCDX2. Two replicates of experimental responses of RAD51 binding at different concentrations are shown by color coded lines. **e**, AlphaFold modeling of the indicated complexes. Two potential RAD51/RAD51B binding modes are presented; mode 1 in which the surface harboring the primary ATP binding site of RAD51B interacts with RAD51, and mode 2 in which the surface harboring the secondary ATP binding site of RAD51B interacts with RAD51. RAD51/

RAD51 interface from the presynaptic complex (PDB: 7EJC) is shown for comparison. Buried surface area (calculated using PISA) of the indicated regions are presented to the right of the model/structure. **f**, BCDX2/RAD51 model 1 in which the ATPase domain of RAD51B (secondary ATP binding surface) packs against RAD51C, and RAD51 packs against the primary ATP binding surface of RAD51B (mode 1). **g**, BCDX2/RAD51 model 2 in which a flexible RAD51B ATPase domain can engage RAD51 through binding modes 1 and/or 2. A cartoon schematic is shown at the bottom.

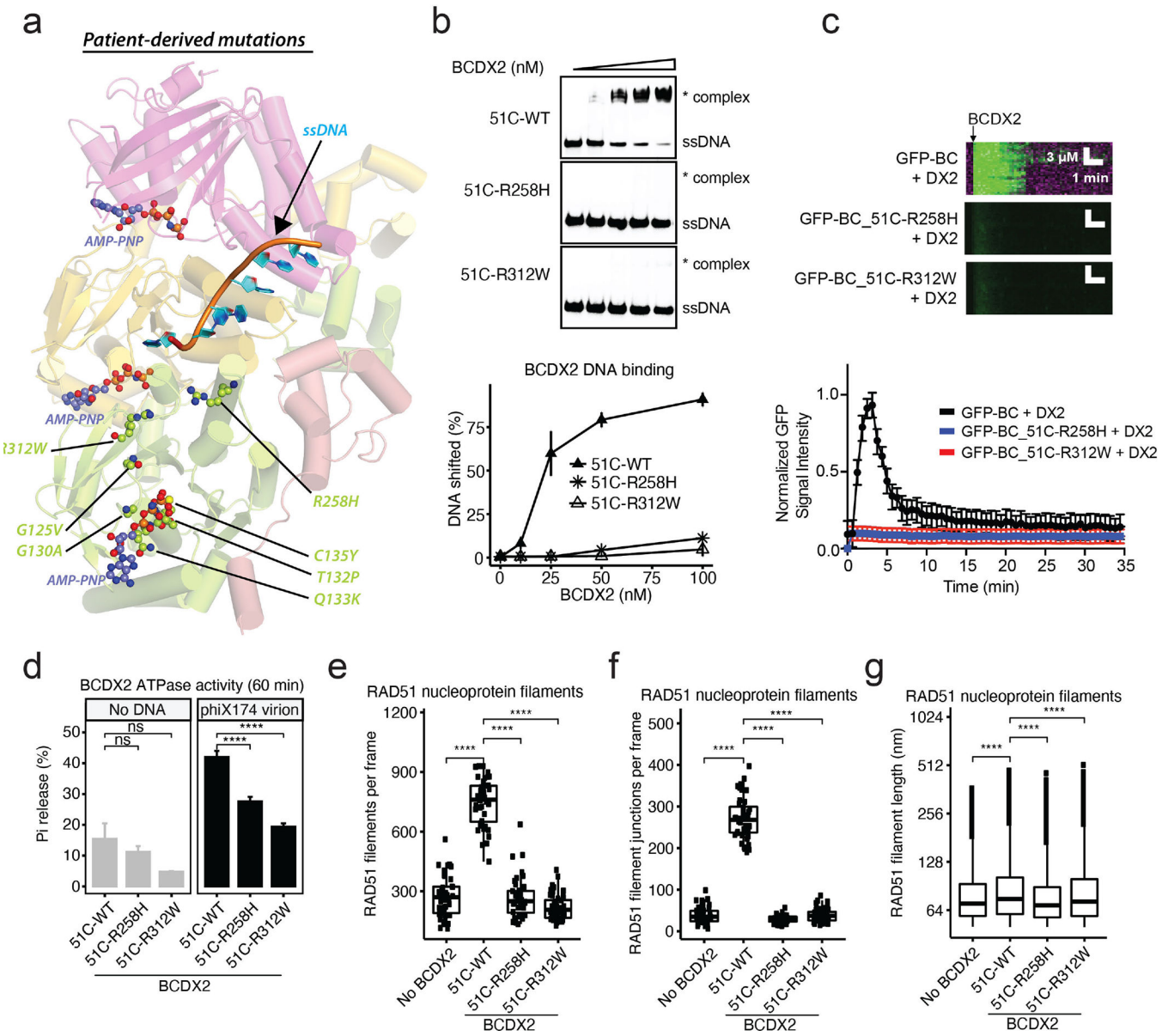

Fig. 7 |. Structural and functional analysis of cancer patient-derived BCDX2 subunit mutations

a, The overall BCDX2/ssDNA structure is shown as a semitransparent cartoon representation with amino acids of cancer patient-derived BCDX2 subunit mutations shown as solid spheres. **b,** ssDNA binding by the WT and indicated mutant BCDX2 complexes were assessed by electrophoretic mobility shift assays using an 80mer substrate and measurements for three independent experiments plotted. **c,** Representative kymographs of single ssDNA molecules (*top*) showing the indicated GFP-BCDX2 variant (10 nM each protein complex) in the presence of 2.5 mM ATP binding to and dissociating from a mCherry-RPA-ssDNA. The graph (*bottom*) shows quantification of GFP-BCDX2 binding to the mCherry-RPA-ssDNA. The kymograph and graph for GFP-BC + DX2 (+ATP) were reproduced from Figs. 5a and b, for comparison. Data are represented as mean normalized GFP signal intensity; error bars represent 95% CI. Data were derived using three flow

cells per reaction condition. **d**, Histograms depicting ATP hydrolysis with 1 μM WT and indicated mutant BCDX2 complexes with or without ssDNA after 60 min incubation and measurements for three independent experiments were plotted. *p*-values were calculated as indicated as in Fig. 3c. **e-f-g**, Box plots depict (**e**) number of RAD51 nucleoprotein filaments per frame, (**f**) number of junctions formed by filaments per frame and (**g**) length of filaments in nanometers measured by negative stain electron microscopy in absence or presence of WT BCDX2 (reproduced from Fig. 5l–m–n, for comparison) or BCDX2 with RAD51C mutants R258H and R312W. *p*-values were calculated as in Fig 5l–m–n.